Theoretical near-field vibrational spectroscopy
理論近接場振動分光学

Masato Takenaka

Graduate School of Chemical Sciences and Engineering

Hokkaido University

March 2021

Contents

1 General Introduction

1.1 Spectroscopy

Spectroscopy is a chemical analysis method that irradiates light onto a material and allows us to determine the properties of the material by measuring the absorption or scattering of the light. The type of light is classified by the wavelength and the physical quantity measured depends on the type of light to be observed. For example, X-ray spectroscopy is used to study the crystal structure of materials.[A1] UV-visible absorption spectroscopy is used to observe electronic excitation[A2], infrared absorption vibrational spectroscopy is used to observe vibrational excitation[A3], and terahertz wave spectroscopy is used to observe molecular rotation.[A4]

1.2 Vibrational spectroscopy

Among others, vibrational spectroscopy[A3] is useful for determining the material structure. A molecule has 3N-6 vibrational modes, where N is the number of atoms. Each vibrational mode is usually localized in a functional group. Since the range of vibrational frequencies for each functional group is determined, the structural information about the molecule can be obtained from the peak positions in the spectrum. Specifically, the region from 600 to 1500 cm^{-1} is called the fingerprint region, and the region over 1500 cm^{-1} is called the diagnosis region. Vibrational spectroscopy is used to analyze various objects because it does not require pretreatment of the sample and is a non-destructive method. The vibrational excitation energy of a molecule is in the infrared region, and there are two types of spectra: infrared absorption (IR) spectra and Raman spectra. The detail of IR and Raman spectroscopy is discussed in each chapter 2,3, and 5. In recent years, the technology in vibrational spectroscopy is progressing fast. Above all, the advancement of nano-spectroscopy, which has a high spatial resolution, is significant with the advances in nanoscience.

1.3 Diffraction limit

Nano-spectroscopy refers to spectroscopy with nanometer spatial resolution. It is an indispensable technique for the structural analysis of nanomaterials and for the observation of chemical reactions at the interface. In nano-spectroscopy, the spatial resolution limit is a problem.[A5] Abbe defined the resolution limit[A6]

$$\Delta r_{\min} = 0.6098(\lambda/\mathrm{NA}) \tag{1}$$

$$\mathrm{NA} = n\sin\theta \tag{2}$$

where NA is the numerical apertures, n is the refraction index of the medium, θ is the angle between the optical axis and the light at the outermost of the effective, and λ is the light wavelength. $\Delta r_{\min}$ is defined as the minimum distance at which two point dipoles can be distinguished by the image, as shown in Fig. 1. Electron microscopes using electron beams can reveal the atomic structure of materials, but the long wavelengths of infrared, ultraviolet, and visible light make it difficult to achieve vibrational spectroscopy at the nanoscale resolution.

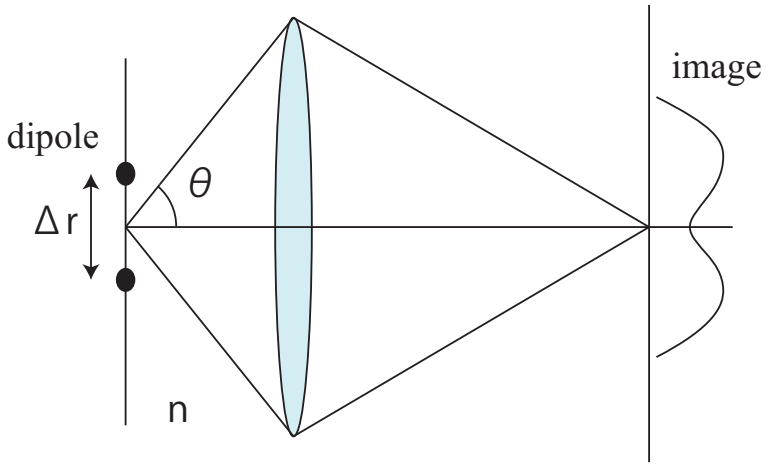

Figure 1: The scheme of Abbe's resolution limit. Δr_{min} is the minimum distance at which two point dipoles can be distinguished by the image.

1.4 Nano-spectroscopy with near-field

One of the methods to overcome the diffraction limit has been developed using the near-field technique.[A7] The near field means localized electric field on the material surface within the light wavelengths or less. By applying such a localized electric field to spectroscopy, we can observe the local response of materials. There are some types of near fields. For example, when light is irradiated on a nanoparticle, a polarization is generated in the nanoparticle, which oscillates at the frequency of the incident light. The polarization of the nanoparticle can be regarded as the oscillation of the dipole moment as shown in Fig. 2(a). The far-field is propagating electric fields away from the light source. It is known that the near-field component of the electric field created

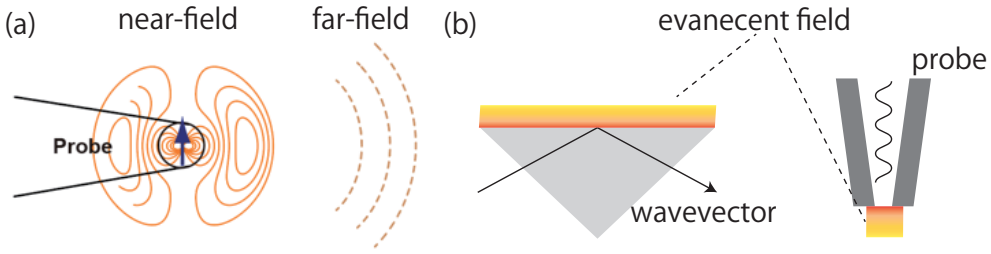

Figure 2: Electric fields around the oscillating dipole.

by the dipole moment decays with respect to the distance r in proportion to r^{-3}. And the spatial extent of the near field is roughly equal to the size of the particle.[A7] On the other hand, when light is totally reflected at the interface between two mediums with different refractive indices, a electric field which decays exponentially is produced at the interface of the low refractive index side at a depth of about the wavelength of the light, as shown in the left of Fig. 2(b). This is called an evanescent field, which is also a type of near field. The evanescent field is also generated at the apex of the aperture probe, as shown in the right of Fig. 2(b). The diameter of the probe is smaller than the light. One of the major application of the aperture probe is scanning near-field optical microscopy(SNOM).[A8] The radiation emerging from the interaction of the probe and sample is observed. The spatial resolution of aperture SNOM reaches within 100 nm.

1.5 Near-field vibrational spectroscopy

The near-field is applied to vibrational spectroscopy combined with the near-field microscopy. A concrete example is the near-field Raman spectroscopy.[A9] However, the measurement of Raman scattering with the aperture probe is only applicable for limited samples, such as pure materials[A10], or in the resonance Raman condition[A11], because of the low signal level which comes from the very small Raman scattering cross section of molecules.[A12]

1.5.1 Plasmon

As a solution to the low Raman signal level at nano-scale, the Raman spectroscopy with plasmon has been developed. Plasmon is a quantized collective oscillation of free electrons, which generates strong near fields around the metal surface.[A5] When the electron distribution shifts from the ground state, the Coulomb force between the nucleus and the electrons act as a restoring force, and thus electrons harmonically oscillates. Surface plasmon resonance (SPR) is the longitudinal wave in which the change in electron density propagates along the surface. SPR cannot be excited from propagating light because of dispersion relations and can be excited by evanescent fields. In metal nanoparticles, it is called localized surface plasmon resonance (LSPR), which can be excited by ordinary propagating light. The intensity of the near-field created by free electrons in the plasmon state is enhanced compared to that of the incident light. The excitation wavelength of the plasmon varies depending on the structure and configuration of the metal nanoparticles. In particular, for gold and silver, the absorption wavelength is in the visible light range.

1.5.2 Plasmon-enahnced vibrational spectroscopy

Plasmon-enhanced vibrational spectroscopy[A13] has been developed for both IR and Raman. The technique of using metal nanoparticles and atomically rough metal surfaces and adsorbing molecules is called surface-enhanced infrared spectroscopy (SEIRAS)[A14] in IR, and surface-enhanced Raman spectroscopy (SERS) in Raman, as shown in Fig

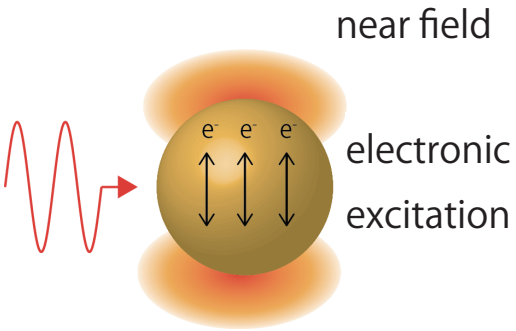

Figure 3: The scheme of localized surface plasmon resonance.

4. SERS was first reported in 1973[A15], and SEIRAS was reported in 1980.[A16] It is known that the peak intensity is strongly enhanced and the enhancement factor is 10^2 to 10^3-fold for SEIRAS and 10^8-fold for SERS.[A3] Tip-enhanced Raman spectroscopy(TERS) uses the metal tip of the scanning tunneling microscope or the atomic force microscope, as shown in Fig. 4, which was reported by several groups in 2000[A17, A18, A19], and scanning near-field infrared microscopy(SNIM) was reported at around the same time[A9], which also uses a metal tip. Recently, single-molecule TERS was achieved.[A20] Furthermore, molecular vibrational mode dependency of the Raman imaging have been reported and it is said that non-uniformity of the near-field is the key to the observation of a single molecule.[A21, A22]

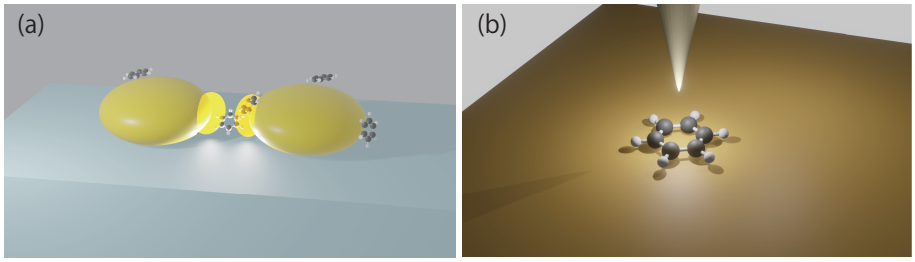

Figure 4: (a)The schematic diagram of surface-enhanced Raman spectroscopy and (b)Tip-enhanced Raman spectroscopy.

1.5.3 Theory of plasmon-enhanced vibrational spectroscopy

Theoretical studies of plasmon-enhanced vibrational spectroscopy have been mainly focused on the mechanism of peak enhancement. The mechanism of peak enhancement has been discussed in terms of physical and chemical enhancement.[A13] The physical enhancement is due to a strong near field around the plasmonic metal. In the case of SERS and TERS, the enhancement factor is known to be proportional to the fourth power of the amplitude of the enhanced electric field $|E|^4$.[A23, A24] The enhancement of SEIRAS has been similarly discussed by the two factors, but the order of magnitude of the enhancement is smaller in SEIRAS. This is because the resonance wavelength of plasmon metals is mainly in the visible region and IR spectra does not involve electronic excitations and resonances as in Raman spectra. In addition to the enhancement, the spectral peak selection rule can break down due to the non-uniformity of electric fields. Furthermore, resonance Raman effect with quadruple excitation for SERS was reported, which is induced by the electric field gradient.[A25] The chemical enhancement mechanism can be divided into three types: molecular resonance mechanisms, charge transfer mechanisms, and non-resonant mechanisms.[A26, A27] The first is molecular resonance mechanism due to resonance Raman effect in the molecule, the second is the charge transfer mechanism due to charge-transfer excitation between the molecule and the metal, and the third is non-resonant mechanism is due to ground state interaction between the molecule and the metal. This classification is widely accepted[A13] and calculated for each mechanism by DFT calculations.

1.6 The present situation of quantum chemistry for near-field excitations

Quantum chemical computational programs which can treat near-field vibrational spectroscopy does not exist up until now. Nowadays, some computational methods for TERS imaging are reported[A28, A29, A30], but the effect of spatial near-field distribution for the Raman scattering is still incompletely understood. In addition, to our best knowledge, few reports are available on computational methods for IR spectra, which consider

the near-field effect.

1.7 Interaction between molecule and near-field

The interaction of near-field for molecules is different from far-field. In the far-field case, the electric fields on the molecule are uniform because the wavelength of light is larger in scale than that of the molecule. Therefore, the interaction can be approximated by the inner product of the dipole moment of the molecule and the electric field vector, which is called the dipole approximation (long-wavelength approximation). However, in the near-field case, higher-order multipole interactions, such as quadruple moment and first derivative of the electric field, should be considered.[A31]

The interaction between the molecule and the near field in the non-relativistic region can be described by the multipolar Hamiltonian, which includes the infinite order of multipole interaction terms.[A32] The detail of the Hamiltonian is described in Chapter 2. Because of the complexity of the spatial structure of the near field, it is not clear what order of multipole terms should be taken into account. However, with the multipolar Hamiltonian, we do not have to worry about the truncation of higher-order terms.

1.8 Purpose

As discussed above, vibrational spectroscopy at the nanoscale is important in molecular science. However, there is no general-purpose computational method to calculate such a vibrational spectrum. Therefore, I develop and apply computational methods for near-field vibrational spectroscopy for further theoretical research.

1.9 Overview

In Chapter 2, the background of the theoretical calculations leading to my developed computational method is described. In Chapter 3, I present the computational method for calculating the IR, which is based on the multipole Hamiltonian and the results of the IRRAS and SEIRAS model calculations of nitro benzoic acids. In Chapter 4, I performed DFT calculations for the gold-silver alloy SERS with the cluster model. I discuss the

spectral change by the difference of metal. In Chapter 5, I present the computational method for near-field Raman spectroscopy and the results of the model calculation of TERS. In Chapter 6, summary and outlook of my works are presented.

Reference

[A1] B. K. Agarwal, *X-ray spectroscopy: an introduction*, volume 15, Springer, 2013.

[A2] A. E. Gillam and E. S. Stern, *An introduction to electronic absorption spectroscopy*, Edward Arnold Publishers, 1954.

[A3] J. Chalmers and P. Griffiths, *Handbook of Vibrational Spectroscopy, 5 volumes set.*, Wiley, 2002.

[A4] K.-E. Peiponen, A. Zeitler, and M. Kuwata-Gonokami, *Terahertz spectroscopy and imaging*, volume 171, Springer, 2012.

[A5] L. Novotny and B. Hecht, *Principles of nano-optics*, Cambridge university press, 2012.

[A6] E. Abbe, Archiv für Mikroskopische Anatomie **9**, 413 (1873).

[A7] 大津元一, **近接場光の基礎**, オーム社, 2003.

[A8] B. Hecht et al., The Journal of Chemical Physics **112**, 7761 (2000).

[A9] C. A. Michaels, S. J. Stranick, L. J. Richter, and R. R. Cavanagh, Journal of Applied Physics **88**, 4832 (2000).

[A10] B. Knoll and F. Keilmann, Nature **399**, 134 (1999).

[A11] D. Alastair Smith et al., Ultramicroscopy **61**, 247 (1995).

[A12] W. Zhang, Z. Fang, and X. Zhu, Chemical Reviews **117**, 5095 (2017).

[A13] R. Aroca, *Surface-enhanced vibrational spectroscopy*, John Wiley & Sons, 2006.

[A14] M. Osawa, K.-i. Ataka, K. Yoshii, and Y. Nishikawa, Applied Spectroscopy **47**, 1497 (1993).

[A15] M. Fleischmann, P. J. Hendra, and A. J. McQuillan, Chemical Physics Letters **26**, 163 (1974).

[A16] A. Hartstein, J. R. Kirtley, and J. C. Tsang, Physical Review Letters **45**, 201 (1980).

[A17] P. Verma, Chemical Reviews **117**, 6447 (2017).

[A18] B. Pettinger, P. Schambach, C. J. Villagómez, and N. Scott, Annual Review of Physical Chemistry **63**, 379 (2012).

[A19] F. Shao and R. Zenobi, Analytical and Bioanalytical Chemistry **411**, 37 (2019).

[A20] R. Zhang et al., Nature **498**, 82 (2013).

[A21] J. Lee, K. T. Crampton, N. Tallarida, and V. A. Apkarian, Nature **568**, 78 (2019).

[A22] R. B. Jaculbia et al., Nature Nanotechnology **15**, 105 (2020).

[A23] L. Silberstein, The London, Edinburgh, and Dublin Philosophical Magazine and Journal of Science **33**, 521 (1917).

[A24] D. V. Chulhai, Z. Hu, J. E. Moore, X. Chen, and L. Jensen, Annual Review of Physical Chemistry **67**, 541 (2016).

[A25] M. Takase et al., Nature Photonics **7**, 550 (2013).

[A26] J. R. Lombardi and R. L. Birke, Journal of Physical Chemistry C **112**, 5605 (2008).

[A27] L. Jensen, C. M. Aikens, and G. C. Schatz, Chemical Society Reviews **37**, 1061 (2008).

[A28] X. Chen, P. Liu, Z. Hu, and L. Jensen, Nature Communications **10**, 2567 (2019).

[A29] P. Liu, D. V. Chulhai, and L. Jensen, ACS Nano **11**, 5094 (2017).

[A30] S. Duan et al., Journal of the American Chemical Society **137**, 9515 (2015).

[A31] A. D. Buckingham, Permanent and Induced Molecular Moments and Long-Range Intermolecular Forces, in *Adv. Chem. Phys.*, edited by J. O. Hirschfelder, volume 12, pages 107–142, Wiley Online Library, 2007.

[A32] D. P. Craig and T. Thirunamachandran, *Molecular Quantum Electrodynamics: An Introduction to Radiation-Molecule Interactions*, Dover, 1998.

2 Theoretical foundations

In this chapter, theoretical background of my computaional methods are described. Starting from Schrödinger equation, the Born-Oppenheimer (BO) approximation, the calculation of the electronic state and the specific method for calculating it, the equations for calculating IR spectra and Raman spectra, and the theory of interaction between molecules and light are summarized.

2.1 Born-Oppenheimer approximation

Schrödinger equation of a molecule which includes N electrons and M nuclei is written by

$$H\Psi = E\Psi \tag{1}$$

$$\begin{aligned} H = &-\sum_{i=1}^{N}\frac{1}{2}\nabla_i^2 - \sum_{A=1}^{M}\frac{1}{2M_A}\nabla_A^2 \\ &-\sum_{i=1}^{N}\sum_{A=1}^{M}\frac{Z_A}{r_{iA}} + \sum_{i=1}^{N}\sum_{j>i}^{N}\frac{1}{r_{ij}} + \sum_{A=1}^{M}\sum_{B>A}^{M}\frac{Z_A Z_B}{R_{AB}} \end{aligned} \tag{2}$$

where M_A is the nuclear mass, Z_A is the nuclear charge, r_{iA} is the distance between electron i and nucleus A, R_{AB} is the distance between nucleus A and B, Ψ is the molecular wave function, E is molecular energy, and H is molecular Hamiltonian. Since the proton in the atomic nucleus is about 1,800 times heavier than the electron, the nucleus can be considered to be at rest when considering the motion of the electron. By erasing the kinetic energy term of the nucleus in the equation, we can write the Schrödinger equation for the electron as follows

$$H_e\Phi_e = E_e\Phi_e \tag{3}$$

$$\begin{aligned} H_e = &-\sum_{i=1}^{N}\frac{1}{2}\nabla_i^2 - \sum_{i=1}^{N}\sum_{A=1}^{M}\frac{Z_A}{r_{iA}} \\ &+\sum_{i=1}^{N}\sum_{j>1}^{N}\frac{1}{r_{ij}} + \sum_{A=1}^{M}\sum_{B>A}^{M}\frac{Z_A Z_B}{R_{AB}} \end{aligned} \tag{4}$$

where E_e is called adiabatic potential energy. The energy surface calculated by changing the position of the nucleus is called the potential energy surface.

The total molecular wave function can be expanded by the eigenfunctions of the electron Schrödinger equation. In calculating the expansion coefficients, if we ignore all terms related to the square of the momentum operator, we obtain the following equation.

$$H_{nuc}\Phi_{nuc} = E_{nuc}\Phi_{nuc} \tag{5}$$

$$H_{nuc} = -\sum_{i=1}^{A} \frac{1}{2}\nabla_i^2 + E_e(\boldsymbol{R}) \tag{6}$$

This equation is regarded as the Schrödinger equation of nuclei. This approximation which ignore the terms about the square of the momentum operator is called BO approximation. The molecular wave function can be expressed as the product of the electron wave function and the nucleus wave function. The motion of nuclei can be categorized into three types: translation, rotation, and vibration. The translation can be separated from rotation and vibration by the Eckart conditions, but vibrations and rotations cannot be completely separated.[B1] The Watson Hamiltonian is well known, which can treat rovibrational states of the molecules on a minimum point of the potential energy surface.[B2] The Hamiltonian is given by

$$H = -\frac{1}{2}\sum_{k=1}^{3N-6} \frac{\partial^2}{\partial Q_k^2} + V(\boldsymbol{Q}) + \frac{1}{2}\sum_{\alpha\beta}^{x,y,z} (J_\alpha - \pi_\alpha)\mu_{\alpha\beta}(J_\beta - \pi_\beta) - \frac{1}{8}\sum_{\alpha}^{x,y,z} \mu_{\alpha\alpha} \tag{7}$$

where $\boldsymbol{Q}$ is the normal coordinate given by

$$\boldsymbol{Q} = \sqrt{m}\boldsymbol{x} \tag{8}$$

where m is the weight of atom and $\boldsymbol{x}$ is the amount of displacement of the nucleus. When we consider a vibrational state, we assume non-rotating molecules ($J = 0$). By introducing approximations that neglects the third term (the Coriolis coupling term) and the last term (the Watson term) of Eq. (7), the Hamiltonian becomes the pure vibrational Hamiltonian. From the above, the molecular Hamiltonian is given by the sum of the electronic Hamiltonian, the vibrational Hamiltonian, and the rotational Hamiltonian.

Therefore, the molecular wave function under the BO approximation can be written as below.

$$|\psi\rangle = |e\rangle\,|\chi\rangle\,|\phi\rangle \tag{9}$$

where $|e\rangle$ is the electronic wave function, $|\chi\rangle$ is the vibrational wave function, and $|\phi\rangle$ is the rotational wave function.

2.2 DFT and Kohn-Sham equation

The Schrödinger equation for many-electron systems obtained by the BO approximation is still difficult to solve. The Hartree-Fock (HF) equation is an approximate calculation method.[B3] By assuming the wave function as a Slater determinant, we can derive the Hartree-Fock equation based on the variational method. The energy difference between the solution of the HF equation and the true Schrödinger equation is called the correlated energy. The post-HF methods, which are called the wave function theory, improve accuracy.[B4]

Another approach is density functional theory (DFT), which is based on the Hohenberg-Kohn theorems. There is a one-to-one correspondence between electron density ρ and energy, and electronic energy can be expressed as a general function of electron density.[B5] For the computational application, several computational approaches of DFT are developed. The most popular one is the Kohn-Sham (KS) equation.

$$\left(-\frac{\nabla^2}{2} + V_{\mathrm{H}}(\boldsymbol{r}) + V_{\mathrm{XC}}(\boldsymbol{r}) + V_{\mathrm{ext}}(\boldsymbol{r})\right)\phi_i(\boldsymbol{r}) = \epsilon_i\phi_i(\boldsymbol{r}) \tag{10}$$

$$\rho(\boldsymbol{r}) = \sum_{i}^{N_{\mathrm{elec}}} |\phi_i(\boldsymbol{r})|^2 \tag{11}$$

where ϕ is KS orbital, V_H is the Hartree potential, and V_{ext} is the external potential. The exact form of the exchange-correlation (XC) functional is not known. There are many XC functional, such as localized density approximation (LDA), which assumes a uniform electron gas, generalized gradient approximation (GGA), which includes the gradient of electron density, and the Hybrid method, which includes GGA and HF exchange terms

with the gradient of electron density. Time-dependent Kohn-Sham equation is written by

$$i\frac{\partial}{\partial t}\phi_i(\boldsymbol{r},t) = \left(-\frac{\nabla^2}{2} + V_{\mathrm{H}}(\boldsymbol{r},t) + V_{\mathrm{XC}}(\boldsymbol{r},t) + V_{\mathrm{ext}}(\boldsymbol{r},t)\right)\phi_i(\boldsymbol{r},t) \tag{12}$$

This equation is based on the Runge-Gross theorem, which shows one-to-one correspondence between the time dependent density and the potential.[B6]

2.2.1 Computational methods for Kohn-Sham equation

There are some computational methods for solving the KS equation. There are various methods with different basis functions used to represent KS orbitals. The Gaussian basis, which mimics atomic orbitals, is commonly used in chemistry, and the plane-wave basis is often used to calculate periodic crystals. There are several methods for calculating excited states, such as linear-response TDDFT based on linear-response theory and the real-time method to describe the evolution of the orbitals in real-time.[B7] In the following sections, we will discuss the real-space method and the real-time method, which are used in Chapter 5.

The real-space DFT is based on the Cartesian space separated by a grid. The Cartesian coordinate differential of the function can be calculated from the value of each point in the space using the difference method [B8] as follows

$$\frac{\partial^2\psi}{\partial x^2} \simeq \sum_{n=-N}^{N} C_n\psi(x_i + nh, y_j, z_k) \tag{13}$$

where h is the grid spacing and N is a positive integer. The advantage of this method is that it can be easily paralleled on a large scale.

The inner-shell wave functions of many-electron atoms have many nodes, and a finer grid is required to represent them in the grid basis as they approach the center of the atom. Since the valence shells are significant in chemistry, it is possible to reduce the computational cost by combining the potential for the valence electrons of the inner-shell electrons and the nucleus as a pseudopotential. The norm-preserving potential[B9] and the ultra-soft pseudopotential[B10] are typical examples of pseudopotentials.

In the real-time method, the KS orbital at the next time is obtained by applying the time evolution operator to the KS orbital at a certain time. The exchange-correlation potential is often used in the ground state form rather than the Adiabatic LDA (ALDA) approximation, ignoring the memory effect.[B11]

2.3 Harmonic approximation

Near the equilibrium structure of a molecule, the adiabatic potential for the displacement of the nucleus can be approximated by a quadratic function, which can be regarded as the Schrödinger equation of the so-called harmonic oscillator, as if the two atoms were connected by a spring. The Schrödinger equation of the one-dimensional harmonic oscillator has an analytical solution, which is written as the Hermite polynomial as follows

$$\psi_n^{\mathrm{HO}}(Q) = N_n H_n(Q') e^{-Q'^2/2} \tag{14}$$

$$N_n = \frac{1}{\sqrt{\pi^{1/2} 2^n n!}} \tag{15}$$

$$Q' = \sqrt{\omega} Q \tag{16}$$

$$H_{n+1} = 2Q' H_n - 2n H_{n-1} \tag{17}$$

$$H_0 = 1 \tag{18}$$

$$H_1 = 2Q' \tag{19}$$

where n is the vibrational quantum number. The Taylor expansion on the reference oscillation for the expected value is as follows.

$$\begin{aligned} \left\langle \psi^{\mathrm{HO}} \middle| A(Q) \middle| \psi^{\mathrm{HO}} \right\rangle = & \left\langle \psi^{\mathrm{HO}} \middle| A(Q_0) \middle| \psi^{\mathrm{HO}} \right\rangle \\ & + \left(\frac{\partial A}{\partial Q} \right)_{Q=Q_0} \left\langle \psi^{\mathrm{HO}} \middle| Q \middle| \psi^{\mathrm{HO}} \right\rangle + \ldots \end{aligned} \tag{20}$$

The zero-order term is the expected value of A in the equilibrium structure, and the first-order term is the product of the normal coordinate derivative in the equilibrium

structure and the expected value of the normal coordinate. This expectation value of the normal coordinate is as follows.

$$\left\langle \psi_{n+1}^{\mathrm{HO}} \,\middle|\, Q \,\middle|\, \psi_n^{\mathrm{HO}} \right\rangle = \left(\frac{1}{2\omega}\right)^{1/2} \sqrt{n+1} \tag{21}$$

$$\left\langle \psi_{n-1}^{\mathrm{HO}} \,\middle|\, Q \,\middle|\, \psi_n^{\mathrm{HO}} \right\rangle = \left(\frac{1}{2\omega}\right)^{1/2} \sqrt{n} \tag{22}$$

$$\left\langle \psi_n^{\mathrm{HO}} \,\middle|\, Q \,\middle|\, \psi_m^{\mathrm{HO}} \right\rangle = 0 \qquad \text{(otherwise)} \tag{23}$$

Under the harmonic approximation, the molecular vibrational wave function is given by the product of the harmonic oscillator wave functions.

2.4 Theory of IR spectroscopy

The infrared absorption of a molecule is represented by the transitions between the vibrational states of the molecule in the particular electronic state due to an external electric field. Under the dipole approximation, the interaction Hamiltonian is represented by the inner product of the dipole moments and the electric field. The transition probability between state i and f is given by Fermi's golden rule as follows

$$W_{fi} = |\, \langle \chi_f \,|\, \langle e_f \,|\, \hat{\boldsymbol{\mu}} \cdot \boldsymbol{E} \,|\, e_i \rangle \,|\, \chi_i \rangle \,|^2 \rho(v_{fi}) \tag{24}$$

where $\rho(v_{fi})$ is the density of photon states per frequency. The electric field is treated as constant and separated from the integration. The expected value of the electronic wave function with the dipole moment operator is called the transition dipole moment $\langle e_f | \, \hat{\boldsymbol{\mu}} \, | e_i \rangle = \boldsymbol{\mu}_{fi}$. In the case of IR spectroscopy, electronic state is same for initial and final states, and transition dipole moment becomes the permanent dipole moment $\boldsymbol{\mu}_e$. The transition probability for the vibrational wave function can be written as follows using the Taylor expansion for the reference coordinate, as shown in the previous section。

$$\langle \chi_f \,|\, \boldsymbol{\mu}_e \,|\, \chi_i \rangle = \langle \chi_f \,|\, \boldsymbol{\mu}_e(\boldsymbol{Q} = 0) \,|\, \chi_i \rangle + \left(\frac{\partial \boldsymbol{\mu}_e}{\partial \boldsymbol{Q}}\right)_{\boldsymbol{Q}=\boldsymbol{Q}_0} \langle \chi_f \,|\, \boldsymbol{Q} \,|\, \chi_i \rangle + ... \tag{25}$$

If we ignore the terms after the second order with respect to $\boldsymbol{Q}$, we find that the transition probability is proportional to the reference coordinate derivative of the dipole moments.

In many quantum chemical computational programs, the absorption coefficient is outputted.

$$Abs = \frac{N_A \pi}{3} \left| \frac{\partial \boldsymbol{\mu}}{\partial \boldsymbol{Q}} \right|^2 \tag{26}$$

where N_A is Avogadro constant. This is derived from Boltzmann distribution and rotational average of the molecules.[B12]

The selection rule for IR spectroscopy is originated from Eq. (24) and is given by Eq. (26). Definitely, the parity of dipole moment is odd, and the vibrational ground state is even. Therefore, the vibrational excited wave function must be added. Under the harmonic approximation, the peak selectivity is defined by the normal coordinate derivative of dipole moment.

2.5 Theory of Raman spectroscopy

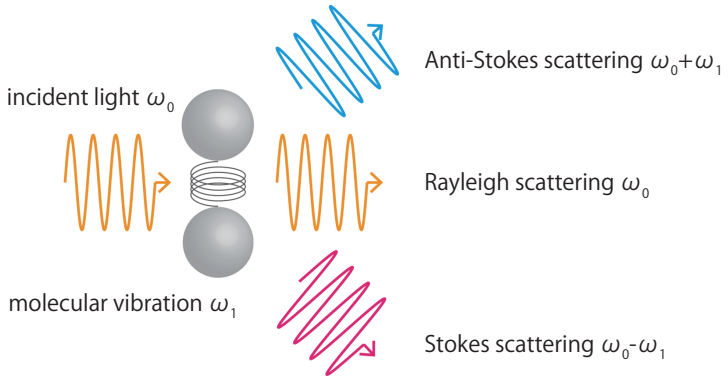

Figure 5: The scheme of Raman scattering.

2.5.1 Classical theory

The scattering of light by a molecule is classically explained as the radiation from the induced dipole moment of the molecule.[B13] The scheme is shown in Fig. 5. The induced dipole moment oscillates at the same frequency and radiates light. This is called Rayleigh scattering. Here, we consider the case when the molecule is vibrating at a certain frequency ω_1. When the molecular structure is distorted by vibration, the induced

dipole moment is modulated. The scattering, which has a frequency shift between the incident light and the molecular vibration, is called Raman scattering. Scattering with a longer wavelength than the incident light is called Stokes scattering, and scattering with a shorter wavelength is called anti-Stokes scattering. By observing the scattered light, we can obtain information about the vibrational mode of the molecule.

2.5.2 Quantum theory

In the quantum theory, Raman scattering is two photon process which consists of absorption and radiation of light. By the second-order time-dependent perturbation theory, Kramers-Heisenberg-Dirac (KHD) equation is derived.[B14, B15]

$$(\alpha_{\rho\sigma})_{fi} = \sum_k \left(\frac{\langle f \,|\, \hat{\mu}_\rho \,|\, k \rangle \langle k \,|\, \hat{\mu}_\sigma \,|\, i \rangle}{E_k - E_i - E_L - i\Gamma} + \frac{\langle f \,|\, \hat{\mu}_\sigma \,|\, k \rangle \langle k \,|\, \hat{\mu}_\rho \,|\, i \rangle}{E_k - E_i + E_L - i\Gamma} \right) \tag{27}$$

where α is the Raman scattering tensor, ρ and σ are any one of x, y, z axis. $|i\rangle$ is initial state, $|k\rangle$ is intermediate state, $|f\rangle$ is final state, E_L is energy of incident light, and Γ is lifetime.

By substituting the product of the electronic wave function and vibrational wave function of Eq. (9) to Eq. (27), α becomes as follows

$$\begin{aligned}(\alpha_{\rho\sigma})_{fi} = \sum_k \sum_{\chi^k} \Bigg(& \frac{\left\langle \chi^f \,\middle|\, \mu_\rho^{fk} \,\middle|\, \chi^k \right\rangle \langle \chi^k \,|\, \mu_\sigma^{ki} \,|\, \chi^i \rangle}{E_{k\chi^k} - E_{i\chi^i} - E_L - i\Gamma} \\ & + \frac{\left\langle \chi^f \,\middle|\, \mu_\sigma^{fk} \,\middle|\, \chi^k \right\rangle \langle \chi^k \,|\, \mu_\rho^{ki} \,|\, \chi^i \rangle}{E_{k\chi^k} - E_{i\chi^i} + E_L - i\Gamma} \Bigg)\end{aligned} \tag{28}$$

where $\mu_\rho^{fk} = \left\langle e^f \,\middle|\, \hat{\mu}_\rho \,\middle|\, e^k \right\rangle$ and $E_{k\chi^k}$ is the sum of electronic energy and vibrational energy of the state k.

When the energy of incident light is far from resonance energy, the vibrational energy of the denominator can be ignored ($E_{k\chi^k} \simeq E_k$). By the resolution of the identity $\sum_k |\chi^k\rangle \langle\chi^k| = 1$,

$$(\alpha_{\rho\sigma})_{fi} = \langle \chi^f | \, \alpha_{\rho\sigma} \, | \chi^i \rangle \tag{29}$$

$$\alpha_{\rho\sigma} = \left(\frac{\mu_\rho^{fk} \mu_\sigma^{ki}}{E_{fi}^{\mathrm{elec}} - E_L - i\Gamma} + \frac{\mu_\sigma^{fk} \mu_\rho^{ki}}{E_{fi}^{\mathrm{elec}} + E_L - i\Gamma} \right) \tag{30}$$

where α the electric polarizability tensor when the initial state and the final state are same. This approximation is called as Placzek's polarizability approximation.[B16] The selection rule of non-resonance Raman spectroscopy is defined by the product of the polarizability and the molecular vibrational wave function.

On the electronic resonance condition, the first term becomes dominant, which is called the resonance term. The second term is called the non-resonance term.

There are some computational method to calculate resonance Raman spectra. Albecht et al. applied perturbation theory to the intermediate electronic state.[B17]

$$|e^k(\boldsymbol{Q})\rangle = |e^k(\boldsymbol{Q}_0)\rangle + \sum_{l\neq k}\sum_v \frac{h^v_{lk}}{E_k - E_l} Q_v \, |e^l(\boldsymbol{Q}_0)\rangle \tag{31}$$

$$h^v_{lk} = \left\langle e^l(Q_0) \middle| \left(\frac{\partial \hat{H}_{\mathrm{elec}}}{\partial Q_v}\right)_{Q=0} \middle| e^k(Q_0) \right\rangle \tag{32}$$

By substituting Eq. (31) to (28), we get new representation of KHD equation considering vibronic interactions. Here I show two main terms by assuming the initial and final state are the same electronic ground state.

$$\alpha_{\rho\sigma} = A + B \tag{33}$$

$$A = \sum_{k\neq i}\sum_{\chi^k} \frac{\mu^{gk}_\rho \mu^{kg}_\sigma}{E_{k\chi^k, i\chi^i} - E_L - i\Gamma} \left\langle \chi^f \middle| \chi^k \right\rangle \left\langle \chi^k \middle| \chi^i \right\rangle \tag{34}$$

$$\begin{aligned} B = &\sum_{e\neq g}\sum_k\sum_v \frac{\mu^{gk}_\rho \mu^{lg}_\sigma h^v_{kl}}{(E_{fi} - E_L - i\Gamma)(E_l - E_k)} \left\langle \chi^f \middle| \chi^k \right\rangle \left\langle \chi^k \middle| Q_k \middle| \chi^i \right\rangle \\ &+ \sum_{e\neq g}\sum_k\sum_v \frac{\mu^{gl}_\rho \mu^{kg}_\sigma h^v_{lk}}{(E_{fi} - E_L - i\Gamma)(E_l - E_k)} \left\langle \chi^f \middle| Q_k \middle| \chi^k \right\rangle \left\langle \chi^k \middle| \chi^i \right\rangle \end{aligned} \tag{35}$$

where A is Franck-Condon (FC) term and B is Hertzberg-Teller (HT) term. The value of A is mainly determined by the overlap integral of vibrational wave functions called as FC factor.

Another approach is based on Taylor expansion of transition dipole moment by normal coordinate.[E56]

$$\mu^{gk}(\boldsymbol{Q})_\rho = \mu^{gk}(\boldsymbol{Q}=0)_\rho + \sum_i j \frac{\partial \mu_\rho^{gk}}{\partial Q_j^g} Q_j^g + \sum_{j,l} \frac{\partial^2 \mu^{gk}}{\partial Q_j^g \partial Q_l^g} Q_j^g Q_l^g + ... \tag{36}$$

Here we assume the only one electronic excited state is considered and vibrational states are direct products of one-dimensional states. By substituting the first and second terms to Eq. (28), we can get next formula.

$$\begin{aligned}
(\alpha_{\rho\sigma})_{fi} = & \sum_{\chi^k} \frac{\mu_\rho^{fk}(0)\mu^{ki}(0)_\sigma \left\langle \chi^f \middle| \chi^k \right\rangle \left\langle \chi^k \middle| \chi^i \right\rangle}{E_{k\chi^k} - E_{i\chi^i} - E_L - i\Gamma} \\
& + \sum_k \frac{\mu^{ki}(0) \left\langle \chi^f \middle| \sum_l \left(\mu_\rho'^{fk}\right)_l Q_l \middle| \chi^k \right\rangle \left\langle \chi^k \middle| \chi^i \right\rangle}{E_{k\chi^k} - E_{i\chi^i} - E_L - i\Gamma} \\
& + \sum_k \frac{\mu^{fk}(0) \left\langle \chi^k \middle| \sum_l \left(\mu_\rho'^{ki}\right)_l Q_l \middle| \chi^i \right\rangle \left\langle \chi^f \middle| \chi^k \right\rangle}{E_{k\chi^k} - E_{i\chi^i} - E_L - i\Gamma} \\
& + \sum_k \frac{\left\langle \chi^f \middle| \sum_l \left(\mu_\rho'^{fk}\right)_l Q_l \middle| \chi^k \right\rangle \left\langle \chi^k \middle| \sum_l \left(\mu_\rho'^{ki}\right)_l Q_l \middle| \chi^i \right\rangle}{E_{k\chi^k} - E_{i\chi^i} - E_L - i\Gamma}
\end{aligned} \tag{37}$$

where $(\mu'_\rho)_j$ is $\frac{\partial \mu_\rho}{\partial Q_j^g}$. The first term is also called the FC term, the second and third term are the FC/HT terms, and the fourth term is the HT term. The computational cost of this formulation is high because the hessian of the excited state is needed. There are some approximations based on Eq. (37). Independent mode displaced harmonic oscillator model (IMDHO) is a widely used method, which assumes normal modes and frequencies of both electronic ground state and excited state are identical, and the only equilibrium position is different.[B19]

2.6 Multipolar Hamiltonian

The multipole Hamiltonian is one of the interaction Hamiltonian between molecules and electromagnetic fields, which consist of the molecular polarization field $\boldsymbol{P}$ and the electric field $\boldsymbol{E}$. as shown in Fig. 6.[B20] It should be noted that in this thesis, all the magnetic

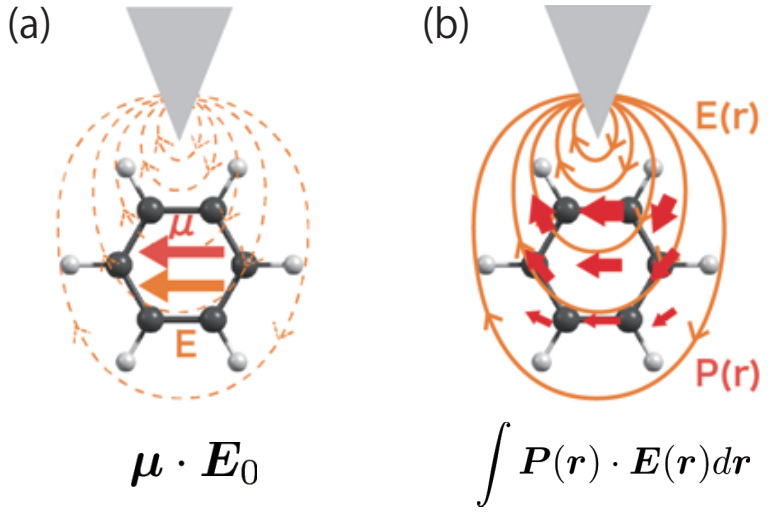

Figure 6: The scheme of (a)dipole approximation and (b)multipolar Hamiltonian.

interactions are omitted, only the electric interactions are considered.

$$H_{\text{mult}} = \int \hat{\boldsymbol{P}}(\boldsymbol{r}) \cdot \boldsymbol{E}(\boldsymbol{r}) d\boldsymbol{r} \tag{38}$$

where $\hat{\boldsymbol{P}}$ is the polarization of the molecule and is defined by the following equation

$$\hat{\boldsymbol{P}}(\boldsymbol{r}) = \sum_{\alpha} e_{\alpha}(\hat{\boldsymbol{q}}_{\alpha} - \boldsymbol{R}) \int_0^1 d\lambda \delta[\boldsymbol{r} - \boldsymbol{R} - \lambda(\hat{\boldsymbol{q}}_{\alpha} - \boldsymbol{R})] \tag{39}$$

where $\boldsymbol{R}$ is the center of gravity of the molecule. This Hamiltonian is a canonical transformation of the minimal coupling Hamiltonian.[B20] Briefly, the transformation is done as $H_{\text{mult}} = \exp(-iS) H_{\text{min}} \exp(iS)$, where $S = (1/\hbar) \int \boldsymbol{P}^{\perp}(\boldsymbol{r}) \cdot \boldsymbol{A}(\boldsymbol{r}) d\boldsymbol{r}$, $\boldsymbol{P}^{\perp}$ is the transverse component of the electric polarization field operator of a molecule, and $\boldsymbol{A}$ is the vector potential.

Reference

[B1] P. R. Bunker, *Molecular Symmetry and Spectroscopy*, Academic Press, 2012.

[B2] J. K. Watson, Molecular Physics **15**, 479 (1968).

[B3] R. February, Proceedings of the Royal Society of London. Series A - Mathematical and Physical Sciences **150**, 9 (1935).

[B4] A. Szabo and N. S. Ostlund, *Modern quantum chemistry: introduction to advanced electronic structure theory*, Courier Corporation, 2012.

[B5] P. Hohenberg and W. Kohn, Physical Review **136**, B864 (1964).

[B6] E. Runge and E. K. Gross, Physical Review Letters **52**, 997 (1984).

[B7] C. A. Ullrich, *Time-dependent density-functional theory: concepts and applications*, OUP Oxford, 2011.

[B8] J. R. Chelikowsky, N. Troullier, K. Wu, and Y. Saad, Physical Review B **50**, 11355 (1994).

[B9] H. R. Hamann, M. Schlüter, and C. Chiang, Physical Review Letters **43**, 1494 (1979).

[B10] D. Vanderbilt, Physical Review B **41**, 7892 (1990).

[B11] M. Petersilka, U. J. Gossmann, and E. K. U. Gross, Physical Review Letters **76**, 1212 (1996).

[B12] J. Neugebauer, M. Reiher, C. Kind, and B. A. Hess, Journal of Computational Chemistry **23**, 895 (2002).

[B13] E. B. Wilson, P. C. Cross, and J. C. Decius, (1980).

[B14] H. A. Kramers and W. Heisenberg, Zeitschrift für Physik **31**, 681 (1925).

[B15] P. A. M. Dirac, Proceedings of the Royal Society of London. Series A, Containing Papers of a Mathematical and Physical Character **114**, 243 (1927).

[B16] G. Placzek, *Rayleigh-Streuung und Raman-Effekt*, Handbuch der Radiologie, Akademische Verlagsgesellschaft, 1934.

[B17] P. Champion, G. Korenowski, and A. Albrecht, Solid State Communications **32**, 7 (1979).

[B18] F. Santoro, C. Cappelli, and V. Barone, Journal of Chemical Theory and Computation **7**, 1824 (2011).

[B19] D. C. Blazej and W. L. Peticolas, The Journal of Chemical Physics **72**, 3134 (1980).

[B20] D. P. Craig and T. Thirunamachandran, *Molecular Quantum Electrodynamics: An Introduction to Radiation-Molecule Interactions*, Dover, 1998.

3 Near-field IR

3.1 Introduction

Infrared (IR) spectroscopy is an indispensable technique to provide fingerprint of various molecules in a non-destructive manner. The applicability of IR spectroscopic techniques is further advanced by using surface plasmon, opening the field of "surface enhanced IR absorption spectroscopy (SEIRAS)" [C1, C2, C3]. Another technique called "surface enhanced IR scattering (SEIRS)" uses a designed surface plasmon as an antenna along with Fano resonance in IR measurements [C4, C5, C3]. Further, for microscopic applications, scanning near-field infrared microscopy (SNIM) facilitates nanometer-scale spatial resolution beyond the diffraction limit [C6, C7, C8, C9, C10], as tip-enhanced Raman spectroscopy, which achieves a very high resolution down to a single-molecule level [C11, C12]. The surface enhanced techniques not only enhance the signal intensity but also provide an understanding of molecular properties at nanometer scale. Further, they can be used to study the behavior of a single molecule if combined with metallic probes. To realize the full potential of these techniques, further understanding based on theoretical and computational frameworks is mandatory.

However, it is not simple to obtain surface enhanced IR spectra computationally. In contrast to conventional spectroscopy based on a laser light or propagating light, the applied electric fields are spatially non-uniform in surface enhanced spectroscopy [C13, C14]. The light-molecule interaction with a propagating light has mostly been studied under the dipole approximation because the wavelength of light in IR or even in visible region is much larger than the molecular size in conventional experiments [C15]. For non-uniform electric fields, the widely available quantum chemistry software cannot calculate the IR spectra because they are based on the dipole approximation. This is even true for just surface spectroscopy such as IR reflection-absorption spectroscopy (IRRAS), where molecules interact with uniform electric field that is polarized along the surface normal direction as shown in Fig. 1a[C16]. In most cases, molecules are assumed to be randomly oriented in a system and interact with incident light. Thus,

the IR spectra can be calculated for molecules isotropically interacting with a uniform electric field. However, a recent study has demonstrated that the field gradient plays a crucial role in determining the spectrum corresponding to surface-enhanced Raman scattering (SERS) [C17]. In plasmon enhanced spectroscopy, molecules interact with an electric near-field highly localized at the nanometer scale. The importance of the field gradient for understanding SERS is also discussed. [C18, C19, C20, C21, C22] In general, the spatial distribution of electric near-field is not unique. Since there are variety of techniques for surface enhanced IR measurements as described above, the experimental setups also have broad spectrum, in which the electric near-field depends on these setups. Thus, we need a more generalized theoretical framework beyond the dipole approximation that is practically tractable with moderate computational cost.

To address this issue, I have developed a computational method to calculate the IR spectra using the multipolar Hamiltonian [C23]. The feasibility of this method was validated by using two cases for IRRAS and SNIM, where I implemented model electric fields. For IRRAS, the electric field was uniform but polarized along the surface normal. For SNIM, I considered the electric field around a metal tip by an electric dipole field. Although the model electric field used here provided a qualitative understanding of surface enhanced spectroscopy, it did not necessarily reproduce the electric field around the metal nanostructure. To this end, numerical calculation of electric field is necessary.

The near-field physics has been intensively studied based on computational electrodynamics, where the Maxwell equations are numerically solved [C14]. Owing to the development of computational electrodynamics software, surface plasmon excitation spectra and/or near-field distribution around nanostructures can now be obtained using routine techniques such as finite difference time-domain (FDTD) technique and finite element method (FEM). It has been observed that the near-field distribution strongly depends on the nanostructure itself. Thus, the near-field should be properly considered to perform molecular computations for surface enhanced IR spectra.

In this study, I propose a method to compute surface enhanced IR absorption in techniques such as SNIM or SEIRAS by combining quantum chemical computation with

classical electrodynamics computation. Electromagnetic calculations were performed to obtain the electric near-field around a metal nanostructure used in experiments, while quantum chemical calculations were performed to compute the electron densities of a molecule in the ground state and the IR signal. The gap between these two methods was bridged by the multipolar Hamiltonian in which an arbitrary electric field could be incorporated.

3.2 Theoretical formulation: IR absorption based on the multipolar Hamiltonian

Here, I briefly review my theoretical framework based on the multipolar Hamiltonian in which a numerically obtained electric field can be incorporated. The detailed derivations and discussions on it can be found in my previous paper.[C23] The linear interaction between the k-th molecular vibration and electric field in terms of the molecular polarization $\boldsymbol{P}(\boldsymbol{r})$ and electric field $\boldsymbol{E}(\boldsymbol{r})$ as follows:

$$V_{\mathrm{int}}^{k} = Q_k \int (\partial \boldsymbol{P}(\boldsymbol{r})/\partial Q_k) \cdot \boldsymbol{E}(\boldsymbol{r}) d\boldsymbol{r} \equiv Q_k \partial V_{\mathrm{int}}/\partial Q_k, \tag{1}$$

where Q_k is the k-th normal coordinate and $V_{\mathrm{int}} = \int \boldsymbol{P}(\boldsymbol{r}) \cdot \boldsymbol{E}(\boldsymbol{r}) d\boldsymbol{r}$. To obtain the generalized IR intensity, We consider the expectation value of V_{int}^{k} using electronic and vibrational wave functions such as $|\Psi_n\rangle |v_i\rangle$

$$\langle v_1| \langle \Psi_0| V_{\mathrm{int}}^{k} |\Psi_0\rangle |v_0\rangle = \langle v_1| Q_k |v_0\rangle \frac{\partial \langle \Psi_0| V_{\mathrm{int}} |\Psi_0\rangle}{\partial Q_k}. \tag{2}$$

Since $\langle v_1| Q_k |v_0\rangle$ is constant under the harmonic approximation [C24], the generalized IR intensity of k-th vibrational mode can be expressed as follows:

$$I_k \propto \left| \frac{\partial A}{\partial Q_k} \right|^2, \tag{3}$$

where

$$A \equiv \langle \Psi_0| V_{\mathrm{int}} |\Psi_0\rangle . \tag{4}$$

Using the exact form of polarization operator,[C25]

$$\hat{\boldsymbol{P}}(\boldsymbol{r}) = \sum_{\alpha} e_{\alpha}(\hat{\boldsymbol{q}}_{\alpha} - \boldsymbol{R}) \tag{5}$$

$$\int_0^1 d\lambda \delta(\boldsymbol{r} - \boldsymbol{R} - \lambda(\hat{\boldsymbol{q}}_{\alpha} - \boldsymbol{R})) \tag{6}$$

where e_α and $\hat{\boldsymbol{q}}_\alpha$ are the charge and the position operator of α-th particle such as an electron or nucleus, the expectation value of $V_{\rm int}$ can be expressed as [C26, C23]

$$\begin{aligned} A &= \langle \Psi_0 | \, V_{\rm int} \, | \Psi_0 \rangle \\ &= -\int \delta\rho(\boldsymbol{r})(\boldsymbol{r} - \boldsymbol{R}) \cdot \boldsymbol{E}_{\rm eff}(\boldsymbol{r}; \boldsymbol{R}) d\boldsymbol{r} \end{aligned} \tag{7}$$

where the electron density difference $\delta\rho(\boldsymbol{r}) = \rho(\boldsymbol{r}) - \rho^{\rm atom}(\boldsymbol{r})$ is defined as the difference between the electron density $\rho(\boldsymbol{r})$ of a molecule and the sum of the electron densities of the neutral atoms $\rho^{\rm atom}(\boldsymbol{r}) = \sum_\alpha Z_\alpha \delta(\boldsymbol{r} - \boldsymbol{R}_\alpha)$ in the molecule, where Z_α and R_α are the charge and position of α-th nucleus, respectively. The SIESTA code utilizes $\delta\rho$ as a main variable. [C27] By using the electron density difference, the molecular polarization made up of the electron and nuclear parts can be summarized into one term. The detailed discussion can be found in my previous papers. [C23]

The effective electric field $\boldsymbol{E}_{\rm eff}$ is defined as follows:

$$\boldsymbol{E}_{\rm eff}(\boldsymbol{r}; \boldsymbol{R}) = \int_0^1 d\lambda \boldsymbol{E}(\boldsymbol{R} + \lambda(\boldsymbol{r} - \boldsymbol{R})), \tag{8}$$

where $\boldsymbol{R}$ is the center of gravity of a molecule. The integral with respect to λ originates from the polarization operator, Eq. (6), where the infinite number of multipoles can be expressed by a compact closed form. By its definition, $\boldsymbol{E}_{\rm eff}$ is an average electric field between points $\boldsymbol{r}$ and molecular center $\boldsymbol{R}$. It should be noted that a molecule interacts with $\boldsymbol{E}(\boldsymbol{r})$ itself, not $\boldsymbol{E}_{\rm eff}$, where the latter appears in my formulation by moving the λ integration from the polarization operator to electric field for numerical applications. The IR intensity given in Eq. (3) is independent of the origin of the coordinate, because it is a difference.

For numerical calculations, the effective electric field is expressed in a finite difference

form as follows:

$$\boldsymbol{E}_{\mathrm{eff}}(\boldsymbol{r};\boldsymbol{R}) = \sum_{i=0}^{M} \frac{1}{M} \boldsymbol{E}\left(\boldsymbol{R} + \frac{i}{M}\boldsymbol{r}\right), \tag{9}$$

where M is the number of points for the numerical integration. IR intensity is calculated by the square of the absolute value of the derivative of Eq. (7) with respect to the normal coordinates. In the present framework to obtain SEIRAS, the calculation of Eq. (9) is needed only once for every $\boldsymbol{r}$ where $\rho(\boldsymbol{r})$ is nonzero.

3.3 Computational details

In this study, I focus on an experiment by Osawa *et al.* [C28], where IR, IRRAS, and SEIRAS spectra for p-nitrobenzoic acid (PNBA) and m-nitrobenzoic acid (MNBA) molecules were reported. Figure 1 shows the scheme of IRRAS and SEIRAS, where the Ag thin film and islands are formed on the CaF_2 substrate, respectively. The molecules are vertically chemisorbed onto the Ag surface, forming a monolayer. The parameters concerning the IR signals used in the present study is based on my previous paper[C23], where the numerical accuracy was tested.

3.3.1 Molecule: Quantum chemical calculations

In the IRRAS and SEIRAS experiments, the CO_2^- group of PNBA and MNBA molecules were vertically chemisorbed onto the Ag surface, while IR spectra were recorded for a PNBA/MNBA-K salt in KBr pellet.[C28] To simulate this, I replaced one H atom from the carboxyl groups of these molecules with Ag_3 for IRRAS and SEIRAS and with K for IR to coincide with the experiment. For IRRAS and SEIRAS calculations, I use a very simple model of PNBA-/MNBA-Ag_3 with bridge configuration as shown in Fig. 6 to reduce the computational cost, which is found to be energetically preferred to with atop configurations by 0.63 eV (see Fig. 2.)

For the adsorption geometries of molecules onto the Ag nanodiscs, PNBA-Ag_{20} are also used to see the preferred adsorption configurations, starting from several initial

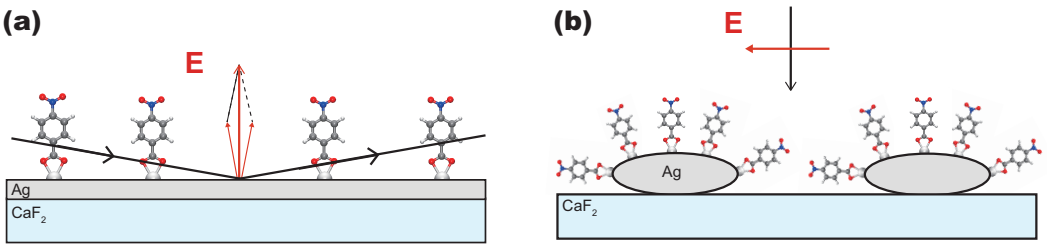

Figure 1: (a) Schematic of IRRAS, where molecules are adsorbed onto the Ag thin film supported by a substrate. The black arrows show the incident and reflected light beams. Red vectors represent the electric fields of the incident and reflected lights and their superposition, creating an electric field polarized normal to the surface. (b) Schematic of SEIRAS, where Ag ellipsoid represents the nanoparticles on a substrate and the molecules adsorbed by the nanoparticles. For molecules, red, blue, gray, and white spheres represent O, N, C, and H atoms. Ag atom is shown by the silver sphere.

geometries, where Ag_{20} of T_d symmetry having four (111) faces. The results for PNBA-Ag_{20} are shown in Fig. 3, which also support that the bridging geometry is preferable. It should be noted that the present calculations were done for neutral systems.

The geometry optimization, generation of electron density difference, and normal modes analysis were performed using a density functional theory code SIESTA [C27] based on Perdew-Burke-Ernzerhof (PBE) functional [C29] and the numerical basis sets of double-zeta plus polarization (DZP) [C30]. The unit cell was calculated to be $25 \times 25 \times 25$ Å. In this size of the unit cell, there were many points at which the electron density was zero, as schematically shown in Fig. 5. For practical applications, however, larger unit cell having enough vacuum area would be desirable in order to neglect intermolecular interactions. Only the gamma point was sampled. The electron density differences were generated on a cube file. The mesh cutoff was set to 200 Ry. Consequently, the unit cell of the system had 216×216×216 points with grid spacing of 0.12 Å. It should be noted

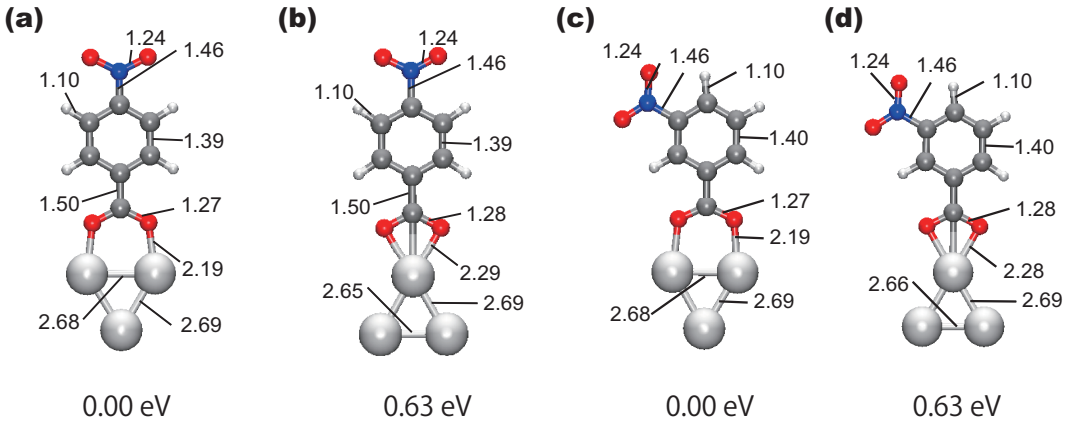

Figure 2: Geometries of (a) PNBA-Ag3 (bridge) (b) PNBA-Ag3 (atop), (c) MNBA-Ag3 (bridge), and (d) MNBA-Ag3 (atop) along with bond length in A and relative total energy in eV shown below the molecules.

that in the present framework, the molecular properties such as geometric and electronic structures as well as the vibrational properties are not affected by the near-field. In the future, I will investigate the effect of IR near-fields on the molecular structure.

3.3.2 Electric field: Electrodynamic calculations

In IRRAS, it is well known that the electric field is polarized along the surface normal due to the interference between the incident and scattered light [C16]. Thus, electrodynamics calculation was not performed. To simulate IRRAS experiment, a uniform electric field parallel to the molecular axes defined by Ag and the nearest C atoms was used. This model has been used in earlier studies to analyze the experimental results in which the derivative of the dipole moment with respect to the normal coordinate was projected to the surface normal [C31].

In contrast, the electric near-field is not generally known in SEIRAS, and thus I computed the scattered near-field around an Ag nanoparticle. The Ag nanoparticle is modeled by an ellipsoid, as shown in Fig. 4, where the major axes (x and y) are parallel to the surface. As shown in Figs. 1(b) and 4, the incident light propagates along the minor axis (z axis) of the ellipsoid and the electric field is polarized along

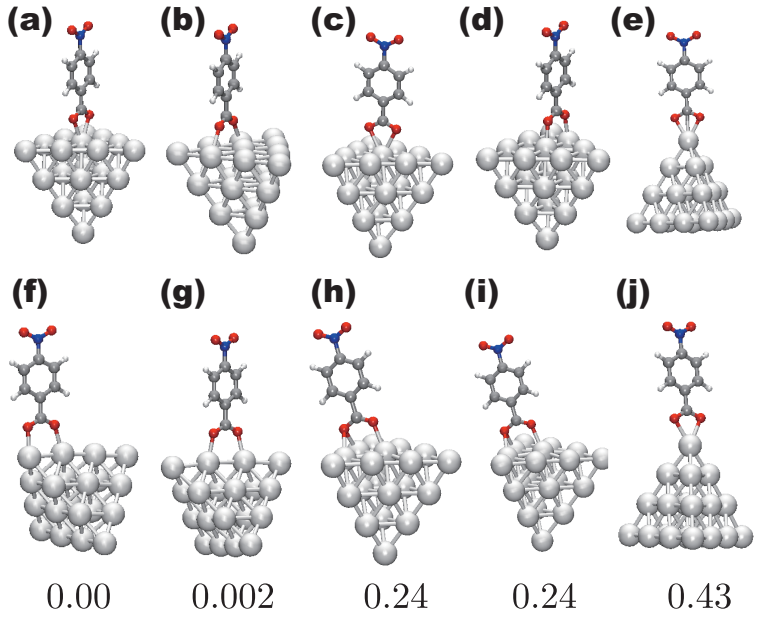

Figure 3: (a-e) Initial and (f-j) optimized structures of PNBA-Ag20 obtained at the level of PBE/def-SV(P) using TURBOMOLE under the resolution of identity (RI) approximation. Relative total electronic energy in eV are shown below the optimized structures. Optimizations are continued until there are no imaginary frequencies. Bridge structures are favored to the atop structures.

the x axis. The intensity of the incident electric field was set to 1 V/μm $\sim 2.7 \times 10^5$ W/cm^2. The scattered electric field around the ellipsoid was calculated by using scuff-em, an open-source software implementation of the boundary-element method (BEM) of electromagnetic scattering for the analysis of electromagnetic scattering problems [C32]. The computational cost with the BEM techniques is smaller than FDTD/FEM methods because BEM only computes the electromagnetic field outside the scatterer. This is an advantage for the present purpose because I need to use very fine grids for calculations of the molecule. The computational mesh of the ellipsoid was automatically generated by gmsh [C33]. Drude model was adopted for the dielectric constant of the Ag [C34]. The electric near-fields were calculated for incident light with wavenumbers of 1000, 1500, and 2000 cm^{-1} to examine the wavenumber dependence of the peak intensity of

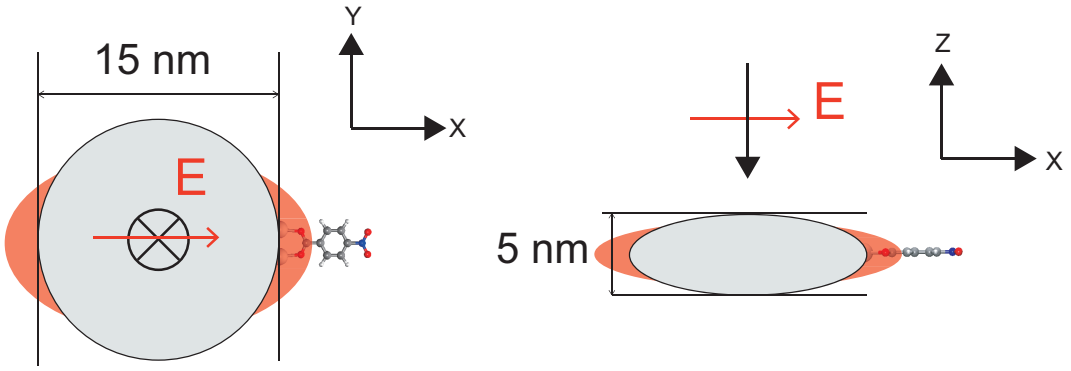

Figure 4: Schema of computational model of SEIRAS. One molecule is adsorbed onto the Ag ellipsoid with a major axis of 15 nm and minor axis of 5 nm.

SEIRAS. It should be noted that the electric field is only calculated for the Ag ellipsoid without adsorbates, even though the adsorbed molecule is shown in Fig. 4 to indicate the configuration of the adsorbate.

3.3.3 Effective electric field

The next step is to calculate the effective electric field $\boldsymbol{E}_{\text{eff}}(\boldsymbol{r})$ using Eq. (9). In the present model for SEIRAS, the midpoint of two bridging Ag atoms and the edges of Ag ellipsoid were matched. The electric near-field was calculated on equally spaced grid points from the center of gravity of the molecular system $\boldsymbol{R}$ to a point $\boldsymbol{r}$. In this study, the number of the grid points was taken as $M = 30$, which was used in my previous study as well [C23]. The effective electric field was not calculated at the points where $\delta\rho(\boldsymbol{r})$ was 0 to reduce the computational cost. In the SIESTA code, as shown in Fig. 5(a), there are many such points because the numerical atomic orbital employed has a cut-off at a certain distance from the atom center where the atomic orbital becomes zero, thereby realizing a sparse density matrix for O(N) calculations [C27]. For the points where $\delta\rho \neq 0$, as shown in colored area in Fig. 5(b), the effective electric field is calculated by using M points from $\boldsymbol{R}$ to $\boldsymbol{r}$. In the present case, I needed to calculate $\boldsymbol{E}(\boldsymbol{r})$ for about 10,000,000 points depending on the molecular systems to obtain $\boldsymbol{E}_{\text{eff}}$. These electrodynamics calculations can be independently performed with the parallel

efficiency of almost 100%.

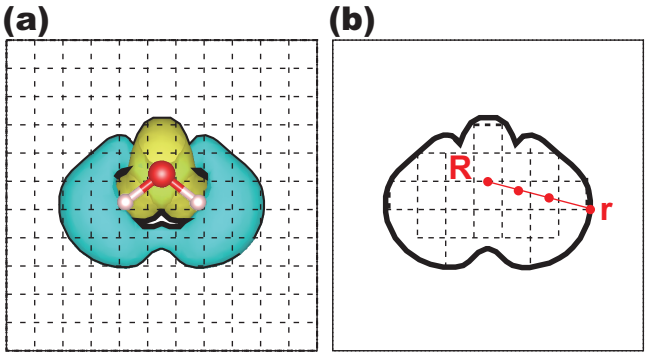

Figure 5: Schema of (a) molecular electron density in the unit cell. The points used for further calculations are color shaded. (b) The schema for the calculation of $\boldsymbol{E}_{\text{eff}}$.

3.3.4 IR spectrum

The normal coordinate derivative of A (Eq. (7)) can be obtained by a matrix transformation from the Cartesian coordinate derivative of A, $\partial A/\partial b_i$, where b_i is the atomic displacements of nucleus in the x, y, z coordinates (i.e., $i = 0...3N$). For the Cartesian coordinate derivative of A, each atomic coordinate was displaced in the positive direction from the equilibrium coordinates by 0.04 a.u. as in my previous study. [C23] The electron density difference was calculated for these shifted structures. Finally, the generalized IR intensity was evaluated by Eq. (3).

3.4 Results and Discussion

The optimized structures of K- and Ag-adsorbed PNBA and MNBA along with the interatomic distances are shown in Fig. 6. The K/Ag-O distance is same for these two molecules, indicating a minor effect of the position of NO_2 group on the other parts including CO_2^- group. From the Bader charge analysis, the charges of the PNBA/MNBA parts for the neutral systems of PNBA-K, PNBA-Ag_3, MNBA-K, and MNBA-Ag_3 are -1.00, -0.71, -1.00, and -0.71, respectively, suggesting that these molecular parts are anionic.

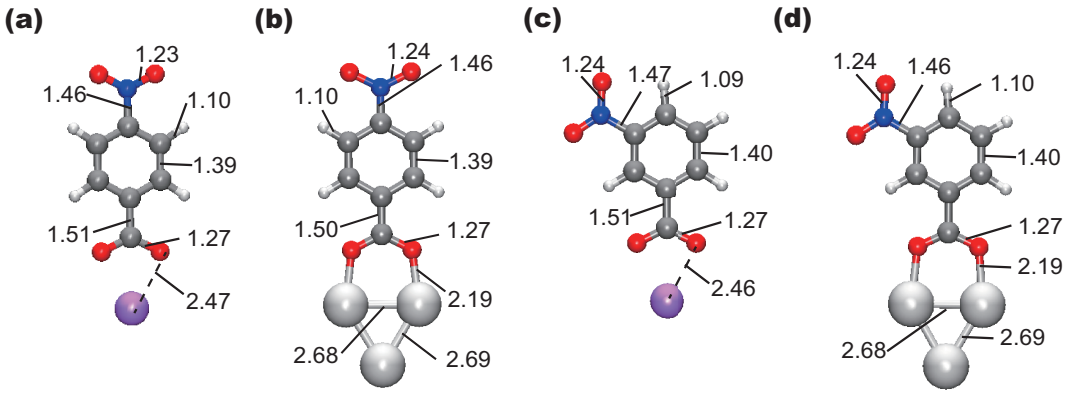

Figure 6: Optimized structures of (a) PNBA-K, (b) PNBA-Ag_3, (c) MNBA-K, and (d) MNBA-Ag_3, along with the bond lengths in Å.

Figure 7 shows the relative intensity and spatial distribution of the near-field around the Ag ellipsoid. The electric field is dipolar. In the relative intensity maps, the incident field strength is considered to be 1. It is evident from the relative intensity map (Fig. 7(a)) that the local electric field at the edge of the particle is strong. The intensity of electric near-field around the Ag ellipsoid is larger than that of the incident field by about 5 times. However, the enhancement was considered as 70 in the experiment [C28]. Therefore, the observed enhancement in the field strength is about an order of magnitude smaller as compared to that reported in the earlier experiment. In the experimental condition, many metal particles exist, and it is considered that the interaction between them may enhance the electric field intensity due to the overlap of near-fields, i.e., an enhancement at gaps between the metal nanoparticles.

Figure 8 shows the electric field over the region of adsorbed molecule at the molecular scale, where the the midpoint of two bridging Ag atoms is set to (x, y, z) = (0, 0, 0). In other words, the surface of the nanoparticle is considered to be at the origin. Figures

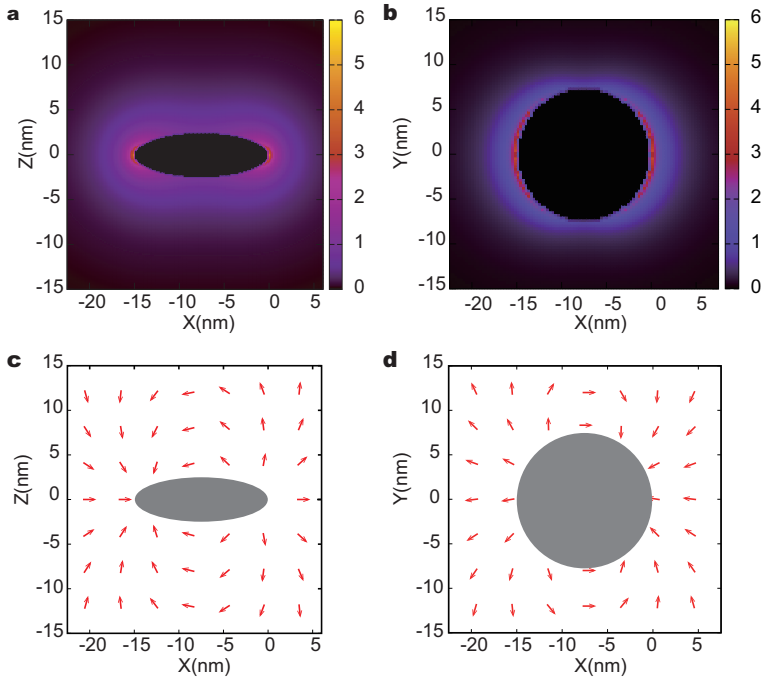

Figure 7: (a) Side and (b) top views of the relative intensity map of the electric near-field. The intensity of incident light is considered as 1. (c) Side and (d) top views of the electric fields around the Ag ellipsoid, shown by the red arrows whose intensity is normalized to show the directions. See axes for Fig. 4.

8(b) and (d) show that the electric fields are almost uniform, and the intensity gradient exists at the molecular scale, which is about 1 nm. The attenuation of $|E|$ is well fitted by $-\ln(x)$ function away from the surface, where x is the distance. This is slower than $1/x$ and much slower than the near-field (longitudinal part) of the electric dipole field, which is proportional to (x^{-3}) [C35, C14]. Compared to the dipole field, the calculated near-field exhibits much weaker intensity gradient, which indicates that the use of dipole field is inadequate and therefore highlights the importance of computational electrodynamics. The field intensity and distribution are unchanged when the wavenumber of the incident light varies as 1000, 1500, and 2000 cm^{-1}, i.e., the near-field is independent of the wavenumber. Therefore, the physical enhancement factor (i.e., the enhancement in the electric field) for SEIRAS is independent of the wavenumber used in the present study.

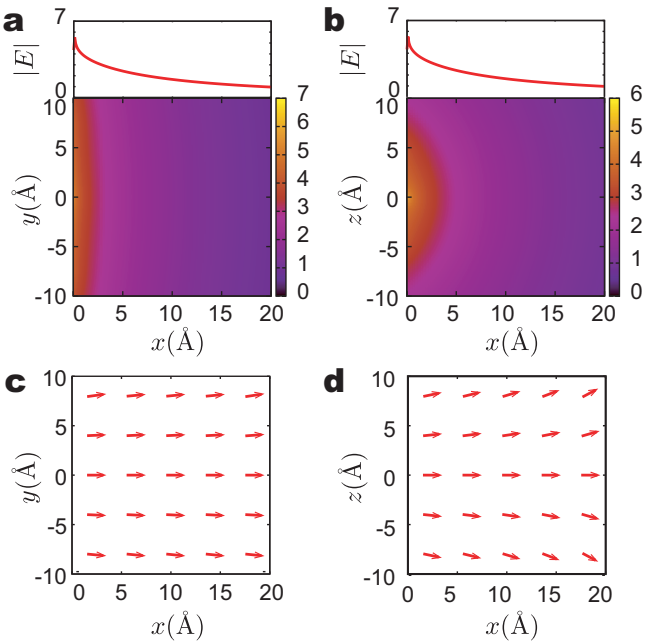

Figure 8: Intensity plot and map for (a) xy-plane at $z = 0$ and (b) xz-plane at $y = 0$. Electric field vectors for (c) xy-plane at $z = 0$ and (d) xz-plane at $y = 0$. The red vectors are normalized just to show the directions.

The computed IR, IRRAS, and SEIRAS spectra of PNBA-K and -Ag_3 are shown in Fig. 9(a), and the assignment and wavenumbers for representative peaks are listed in Table 1. These values are the raw frequencies obtained under harrmonic approximation, which generally overestimate the vibrational frequencies. The overestimation could be corrected by taking account of anharmonicity. PNBA-K and PNBA-Ag_3 show similar vibrational frequencies and coordinates. The peaks 1 and 2 in the IR spectra disappear in the case of IRRAS and SEIRAS. The derivative of the dipole moment with respect to the k-th normal coordinate, $\partial\vec{\mu}/\partial Q_k$, for each vibrational mode is shown by a red arrow in Fig. 9(b). This suggests that the peaks disappear because $\partial\vec{\mu}/\partial Q_k$ is almost orthogonal to the electric field. On the contrary, the derivative of the dipole moment for peaks 3 and 4 are parallel to the electric field, and these peaks are observed in the spectra corresponding to IRRAS and SEIRAS. The peak disappearance is not caused by changing counter-cation/substrate from K to Ag_3. To show this, IR, IRRAS, and SEIRAS of

PNBA-Ag are shown in Fig. 10 where the same system is used to compare these spectra. My computational results are in excellent agreement with the experimental results.[C28] Accordingly, I infer that the present method can be used to study the surface selection rule, where only the vibrational modes whose dipole-moment derivative vector is perpendicular to the surface are allowed for IRRAS and SEIRAS. My method is based on the first-principles calculations, and thus it can be used to analyze more complex molecules without any symmetry, whose adsorption configurations are unknown.

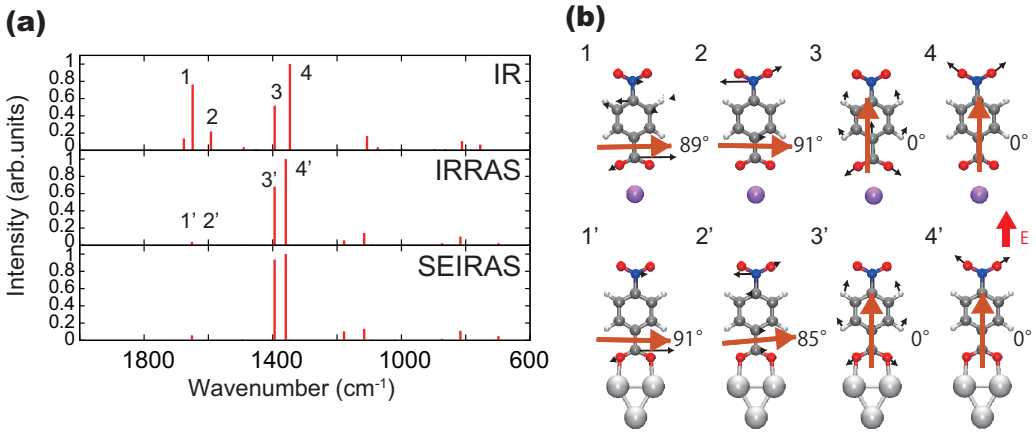

Figure 9: (a) IR and IRRAS and SEIRAS spectra of PNBA-K and PNBA-Ag_3, respectively, from top to bottom. (b) Vibrational modes of peaks 1-4 and 1'-4'. Red arrows show the normal coordinate derivatives of the dipole moment vectors, and the angles relative to the electric field are shown alongside.

Similarly, the result for MNBA is shown in Fig. 11. Here, peak 1 corresponds to an antisymmetric stretching vibrational mode of CO_2. In the case of IRRAS and SEIRAS, this peak disappears because the vibrational mode is tilted by 87 and 108 degrees with respect to the electric field for MNBA-K and MNBA-Ag_3, respectively. In the experiment, this missing peak is assigned to the same CO_2 vibrational mode. Again, the computational result agrees with the Osawa's experimental result. [C28]

Table 2 compares the intensity of the strong peaks 3 and 4 (Fig. 7) obtained by IRRAS and SEIRAS. They represent symmetric stretching vibrations of CO_2 and NO_2,

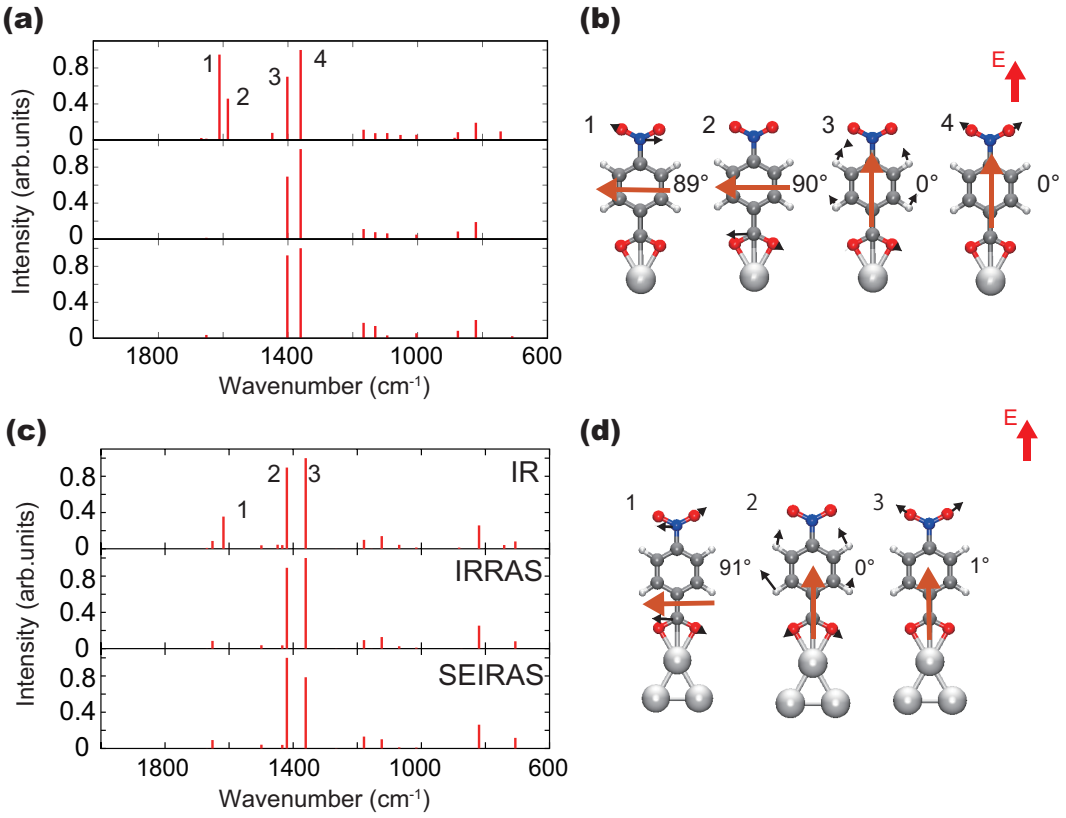

Figure 10: IR, IRRAS, and SEIRAS spectra and representative vibrational mode along with the $\partial\boldsymbol{\mu}/\partial\boldsymbol{Q}$ vectors for (a-b) PNBA-Ag and (c-d) PNBA-Ag_3 of atop configuration, respectively.

respectively. For PNBA, the ratio of the intensities of peaks 3 and 4 in the experiment is reversed in SEIRAS as compared to that in IRRAS. Further, the same trend is observed for MNBA. It is considered that the intensity gradient affects the intensity ratio because the peak of CO_2 is stronger in SEIRAS than in IRRAS. The integrated intensity ratio was evaluated by the spectral area from the previous report. [C28] It may be noted that the computed intensity ratios do not match with the experimental results. The intensities should be decreased and increased for the peaks 3 and 4, respectively, from IRRAS to SEIRAS because the vibration motions are close to and far from the metal surface. Therefore, the most probable origin of the discrepancy is the lack of total absorbance of

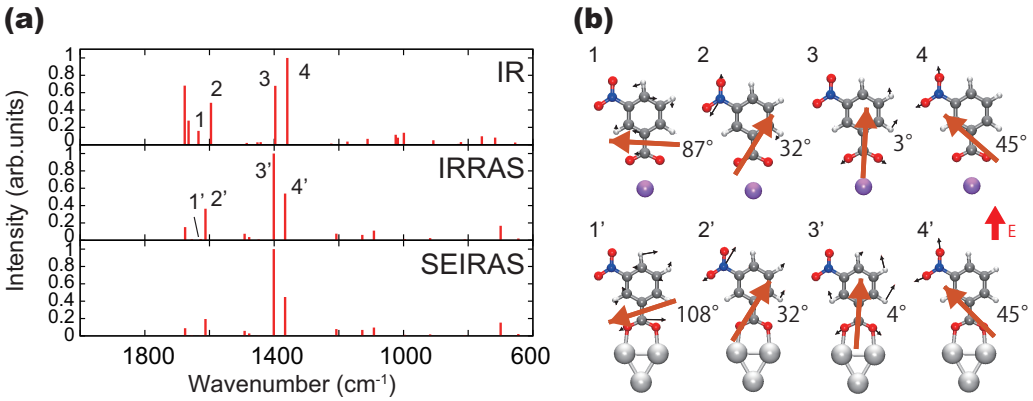

Figure 11: (a) IR and IRRAS and SEIRAS spectra of MNBA-K and MNBA-Ag_3, respectively, from top to bottom. (b) Vibrational modes of peaks 1-4 and 1'-4'. Red arrows show the normal coordinate derivatives of the dipole moment vectors, and the angles relative to the electric field are shown alongside.

the system including the metal. Meanwhile, another reason may be attributed to the use of one metal atom for the adsorption on a surface. The use of surface itself can provide more accurate and quantitative results, but this necessitates treating the surface with periodic boundary conditions, which forms the future scope of this study.

3.5 Conclusion

I have developed a computational method for analyzing surface enhanced IR absorption by incorporating electrodynamic calculations in my quantum chemical model based on multipolar Hamiltonian. The practicality of this model was validated by examining IR, IRRAS, and SEIRAS spectra of small molecules. For SEIRAS, the electric near-field around the Ag ellipsoid has been calculated by boundary element method. The local electric near-field is strong around the edge of the ellipsoid, and the field is polarized along the surface normal. The computed spectra based on these electric fields have reproduced the IR spectra as well as the selection rule of IRRAS and SEIRAS. The present method is based on first-principles calculation and therefore exhibits immense potential to investigate unknown and more complex molecules if metal nanostructures

Table 1: Calculated and experimental wavenumbers of vibrational modes of PNBA-K and PNBA-Ag_3 in cm^{-1}. In the experiment [C28], two peaks with higher wavenumbers are missing due to the selection rule for IRRAS and SIERAS.

	Calc. PNBA-		Experiment [C28]		
Assignment	K	Ag_3	IR	IRRAS	SEIRAS
$V_s(NO_2)$	1347	1359	1345	1351	1338
$V_s(COO^-)$	1394	1394	1383	1388	1387
$V_{as}(NO_2)$	1592	1605	1515		
$V_{as}(COO^-)$	1649	1625	1577		

Table 2: Integrated intensity ratio of the peaks 3' and 4' from Figs. 9 and 11.

		PNBA		MNBA	
Peak number		3'	4'	3'	4'
IRRAS	Expt. [C28]	1.0	0.9	1.0	0.6
	Calc.	1.0	1.4	1.0	0.5
SEIRAS	Expt. [C28]	1.0	1.3	1.0	1.4
	Calc.	1.0	1.1	1.0	0.4

used to enhance the electric field are characterized.

Reference

[C1] A. Hartstein, J. R. Kirtley, and J. C. Tsang, Physical Review Letters **45**, 201 (1980).

[C2] M. Osawa, Bulletin of the Chemical Society of Japan **70**, 2861 (1997).

[C3] F. Neubrech, C. Huck, K. Weber, A. Pucci, and H. Giessen, Chemical Reviews **117**, 5110 (2017).

[C4] F. Neubrech et al., Physical Review Letters **101**, 157403 (2008).

[C5] P. Biagioni, J.-S. Huang, and B. Hecht, Reports on Progress in Physics **75**, 24402 (2012).

[C6] B. Knoll and F. Keilmann, Nature **399**, 134 (1999).

[C7] R. Hillenbrand, T. Taubner, and F. Keilmann, Nature **418**, 159 (2002).

[C8] T. Taubner, R. Hillenbrand, and F. Keilmann, Applied Physics Letters **85**, 5064 (2004).

[C9] M. B. Raschke et al., ChemPhysChem **6**, 2197 (2005).

[C10] E. Bründermann and M. Havenith, Annual Reports Section "C" (Physical Chemistry) **104**, 235 (2008).

[C11] J. Steidtner and B. Pettinger, Physical Review Letters **100**, 236101 (2008).

[C12] R. Zhang et al., Nature **498**, 82 (2013).

[C13] S. A. Maier, *Plasmonics: fundamentals and applications*, Springer Science & Business Media, 2007.

[C14] L. Novotny and B. Hecht, *Principles of nano-optics*, Cambridge university press, 2012.

[C15] G. C. Schatz and M. A. Ratner, *Quantum Mechanics in Chemistry*, DOVER PUBLICATIONS, INC., Mineola, New York, dover edit edition, 2002.

[C16] F. Hoffmann, Surface Science Reports **3**, 107 (1983).

[C17] J. K. Sass, H. Neff, M. Moskovits, and S. Holloway, The Journal of Physical Chemistry **85**, 621 (1981).

[C18] J. K. Sass, H. Neff, M. Moskovits, and S. Holloway, The Journal of Physical Chemistry **85**, 621 (1981).

[C19] E. J. Ayars, H. D. Hallen, and C. L. Jahncke, Physical Review Letters **85**, 4180 (2000).

[C20] P. K. Jain, D. Ghosh, R. Baer, E. Rabani, and A. P. Alivisatos, Proceedings of the National Academy of Sciences **109**, 8016 (2012).

[C21] D. V. Chulhai and L. Jensen, The Journal of Physical Chemistry C **117**, 19622 (2013).

[C22] L. Meng, Z. Yang, J. Chen, and M. Sun, Scientific Reports **5**, 9240 (2015).

[C23] T. Iwasa, M. Takenaka, and T. Taketsugu, The Journal of Chemical Physics **144**, 124116 (2016).

[C24] P. C. Cross, E. B. Wilson, Jr., and J. C. Decius, *MOLECULAR VIBRATIONS: The Theory of Infrared and Raman Vibrational Spectra*, Dover Publications, Inc., N.Y., 1955.

[C25] D. P. Craig and T. Thirunamachandran, Molecular Quantum Electrodynamics: An Introduction to Radiation-Molecule Interactions, 1998.

[C26] T. Iwasa and K. Nobusada, Physical Review A **80**, 043409 (2009).

[C27] J. M. Soler et al., Journal of Physics: Condensed Matter **14**, 2745 (2002).

[C28] M. Osawa, K.-i. Ataka, K. Yoshii, and Y. Nishikawa, Applied Spectroscopy **47**, 1497 (1993).

[C29] J. P. Perdew, K. Burke, and M. Ernzerhof, Physical Review Letters **77**, 3865 (1996).

[C30] J. Junquera, Ó. Paz, D. Sánchez-Portal, and E. Artacho, Physical Review B **64**, 235111 (2001).

[C31] T. Iwasa et al., The Journal of Physical Chemistry C **115**, 16574 (2011).

[C32] M. T. H. Reid and S. G. Johnson, IEEE Transactions on Antennas and Propagation **63**, 3588 (2015).

[C33] C. Geuzaine and J.-F. Remacle, International Journal for Numerical Methods in Engineering **79**, 1309 (2009).

[C34] P. B. Johnson and R. W. Christry, Physical Review B **6**, 4370 (1972).

[C35] J. D. Jackson, Classical electrodynamics, 1999.

4 Theoretical study of surface enhance Raman spectroscopy with alloyed metal

4.1 Introduction

Surface enhanced Raman scattering (SERS) is one of the attractive techniques for molecular detection and has a wide range of applications in bio-medical, food and water safety, security and forensic fields [D1, D2, D3, D4, D5] due to its high sensitivity down to a single molecule detection level.[D6, D7, D8] To gain insight into fundamental SERS mechanisms, it is important to separately consider two different enhancement mechanisms, where a physical enhancement (PE) due to electro-magnetic light field enhancement on the plasmonic metal (Au, Ag, Cu) occurs simultaneously with a chemical enhancement (CE), which results from the formation of bond between the analyte molecule and the surface atoms.[D9] Establishment of such a bond creates a real energy level in the energy diagram of Raman scattering while usually a virtual molecular state is involved when no such bond is present. The opto-mechanical description of SERS with a mechanical oscillator (molecule) coupled to the plasmonic cavity mode entails both: the field enhancement and chemical bonding related mechanisms. [D10, D11] Thereby, PE and CE contributions to SERS can be used in conjunction to maximize detection sensitivity in SERS and is active field of research. In this pursuit rigorously defined SERS structures patterned using high sub-10 nm resolution lithography are suitable to investigate intricate SERS behavior, particularly while maintaining control over PE.[D12, D13]

Recently, scaling rules of SERS intensity on the optical extinction of nano-disc arrays revealed that the strongest extinction does not necessarily to create the strongest Raman scattering. [D12] PE is governed by nano-disc size dependent contributions to scattering and absorption which both contribute to the extinction. The PE can be further increased by exploring the back-side geometry of SERS measurements when the excitation light traverse nano-particles from glass to air (high-to-low refractive index). [D14] Fresnel formulas define the phase changes for reflected and transmitted light and show that 3-10 times higher SERS signal can be obtained on the typical dielectric substrates of refractive

index 1.5-2.7 when back-side SERS excitation is used. [D14] Resonant energy transfer between nano-particles coated with a precisely defined dielectric layer is one more method to exert precise control over PE in SERS [D15] as well as to control separation of self-assembled nanoparticles with a 1-3 nm precision via DNA tethers. [D16]

The CE contribution to SERS deserves a particular interest for creation of analyte specific SERS substrates on which Raman signal can be enhanced by orders of magnitude due to creation of a real energy level, hence resonant SERS. The CE factors ranging from 100 to 1000 times have been demonstrated.[D17, D18] For better understanding of CE mechanisms experiments were carried out using small analyte molecules, which have numerous ways of bonding to the Au, Ag, or Au-Ag alloy. Such alloy systems of coinage metals (Au, Ag, Cu) have a broader range of applications, beyond those of pure Au.[D19, D20, D21, D22] The interaction between 22BPY and metal is mostly discussed in the context of coordination chemistry. [D23] Free 22BPY can take trans conformation and coordinated 22BPY takes cis conformation. On the surface adsorption, monolayer of 22BPY on metal surface is studied by SERS under the applied electric voltage. [D24, D25] In these studies, adlayer of 22BPY on Au(111) seems to consist of cis conformation taking advantage of a lateral π stacking interaction. For Ag surfaces, the orientation at surface investigated can be changed from parallel to perpendicular to the surface depending the applied field, [D26] in which theoretical study is also performed with Ag_{10} pyramidal cluster model. Although there are many experimental studies, theoretical study on the structural and electronic properties of 22BPY adsorbed on metal surface is not so many and not reported yet on a Au-Ag alloy. To understand the complicated SERS behavior with Au-Ag alloy cited above, one has to study the adsorption of 22BPY to the alloy in the first place.

In this study, to understand SERS spectral variations between Au, Ag and its alloy Au-Ag systems, structural and electronic properties of Au, Ag, and Au-Ag alloy clusters and adsorption of 22BPY to these clusters are investigated by means of density functional theory (DFT) computations for considering the CE effect. The effects of metal alloy on DFT modeled Raman scattering bands were considered by conducting simulations for 20-

atom clusters with different compositions. The DFT modeled Raman bands of alloyed and pure Ag and Au metals are expected to have only qualitative resemblance with experimental spectra due to PE which is material, shape, size, and ambient dependent. A qualitative explanation of SERS and CE mechanisms has been obtained and provides insight to SERS mechanisms acting in the range from atomic to nanoscale dimensions. The detail of the experimental setup and the results are written in our paper.[D27]

4.2 Computational detail

To gain insight into the vibrational properties of 22BPY adsorbed on nanodiscs of Au, Ag, and Au-Ag alloy, a widely-used model of 22BPY adsorbed on clusters Au_{20}, Ag_{20}, $Au_{10}Ag_{10}$ were studied.[D18] For these systems the spin-restricted density functional computations were performed at the B3LYP-D3 level [D28, D29, D30] with the Resolution of Identity approximation,[D31] using the def-SV(P) basis sets [D32] as implemented in TURBOMOLE. [D33, E48] Raman spectra were computed using the dynamic polarizability gradient obtained with the EGRAD module [D35, D36] for the excitation wavelength of 785 nm for comparison with experimental SERS measurement results. The line spectra were convolved with a Lorentzian of 10 cm^{-1} width. With the present level of theory, a simulated Raman spectrum was well matched to the experimental Raman spectrum of 2,2'-Bipyridyl. [D26]

4.3 Results and discussion

Figure 1 shows the optimized structures of pyramidal Au_{20}, Ag_{20}, and $Au_{10}Ag_{10}$ clusters. There are in principle ${}_{20}C_{10} = 184,756$ types of alloy clusters, but it is impossible to consider all these structural isomers and in this study I only consider six types of alloy clusters to see how the variations in the alloy geometry affect the adsorption and vibrational properties of 22BPY. Although theoretical studies are found for smaller sizes of Au-Ag alloy clusters,[D37, D38] theoretical analysis on the 20-atom alloy is not reported yet to the best of my knowledge. Figure 2 plots the bond distances for these clusters and experimental lattice constants obtained from powder X-ray diffraction spectroscopy.

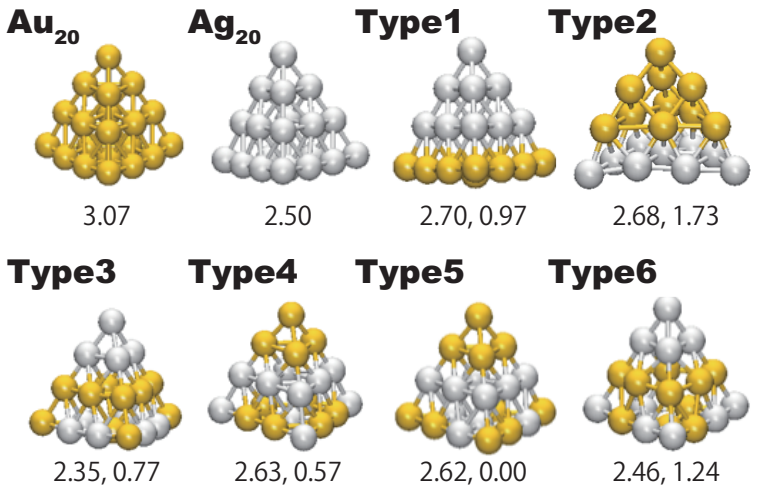

Figure 1: Optimized structures of pyramidal Au_{20}, Ag_{20}, and six types of $Au_{10}Ag_{10}$ alloy clusters along with HOMO-LUMO gap energy in eV, as well as relative total energies in eV for the alloy clusters.

Experimentally the Au-Au distance in general is shorter than Ag-Ag, that is comparable for interatomic distances for Au-Ag alloy of 50-50 %, the present cluster model show rather variations in the bond distances because of the large surface ratio. Au_{20} of this structure is known as a magic number cluster and therefore has large HOMO-LUMO gap energy. This is also true for Ag_{20} and $Au_{10}Ag_{10}$ alloys because the total number of valence electrons is the same. For alloy clusters, segregated structures of Types 1 and 2 has rather low stability than the lowest energy one, Type 5. The Ag(111) face of Type2 is bowed perhaps to compensate the deformation coming from shorter Ag-Ag distances than Au-Au distances, as shown in Figure 2a. For these M_{20} clusters, next I investigate the adsorption or 22BPY.

Figure 3 shows the optimized structures of 22BPY-M_{20} along with the relative total energies for each column. The binding energy is estimated by $E_{\rm tot}(22{\rm BPY}^{\rm cis/trans} - {\rm M}_{20}) - E_{\rm tot}(22{\rm BPY}^{\rm cis/trans}) - E_{\rm tot}({\rm M}_{20})$, where $E_{\rm tot}$ is the total energy. In general, the planar adsorption of trans-22BPY is preferred and cis-22BPY bind to the (111) surface with N-Ag bond is energetically very close to the lowest energy one. The different

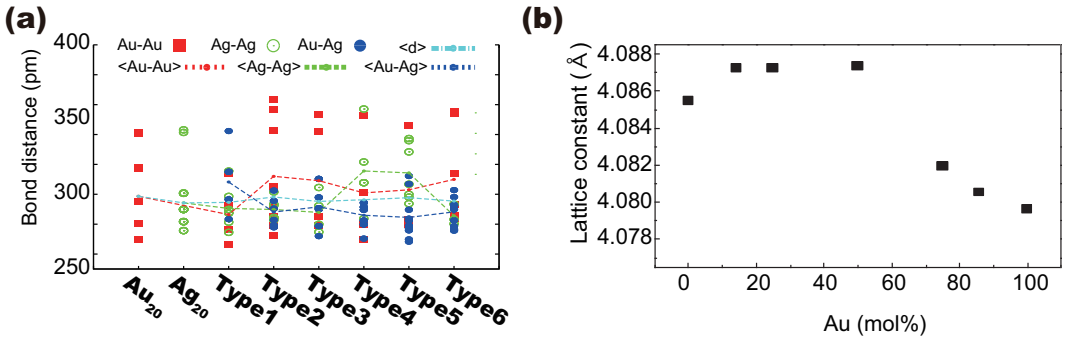

Figure 2: (a) Plot of bond distances of Au-Au, Au-Ag, and Au-Ag and their averages of ⟨Au-Au⟩, ⟨Ag-Ag⟩, ⟨Au-Ag⟩, and ⟨d⟩, where d is all the distances for the optimized structures shown in Figure 1. (b) Experimental lattice constants obtained from Powder X-ray diffraction spectroscopy for Au-Ag alloys with different molar ratio.

order of the relative energy and binding energy comes from the total energy difference between cis- and trans-22BPY, where the trans conformation is more stable by 0.33 eV. It is found that the binding energy to pure Au is larger than pure Ag and Au-Ag alloy in this model. Adsorption of cis-22BPY to the (111) face of M_{20} clusters, N of 22BPY preferably binds to Ag than to Au. This difference causes the different binding motifs and this can cause the different Raman signals of 22BPY. Also, the alloy surface can be deformed compared to the pure metal surfaces, which can roughen the alloy surface giving rise to multiple molecular binding sites and binding conformations.

To see the nature of different affinities of inter-metal and 22BPY to metal atoms, I studied bonding energies of diatomic molecules and the results are in the following order; Au-Au (1.84 eV), Au-Ag (1.82 eV), and Ag-Ag (1.51 eV). Because Ag-Ag bond is rather weak compared to Au-Au and Au-Ag, Ag atoms surrounded by Ag atoms can relatively easily be lifted up making Ag-N bond. The bonding energies between 22BPY and Au/Ag with N-Au/Ag bond are in the following order; cis-22BPY–Au (0.61 eV), cis-22BPY–Ag (0.56 eV), trans-22BPY–Au (0.41 eV), and trans-22BPY–Ag (0.31 eV). Bonding with cis-22BPY is stronger than trans-22BPY. Comparisons between inter-metal bond and metal-22BPY bonds are not trivial but from the structures of 22BPY-M_{20}, Au-Au bonds

seem to be preferred to other interactions, perhaps because of the aurophilic interaction. [D39]

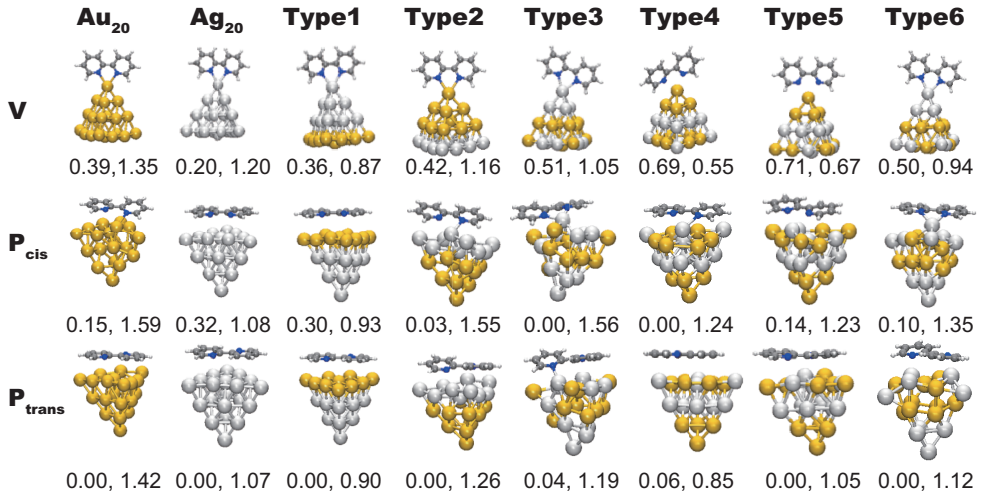

Figure 3: Optimized structures for 22BPY-M_{20} (M=Au/Ag) and relative total energy in eV for each column and binding energy in eV of 22BPY estimated to be the total energy difference between 22BPY-M_{20} and M_{20} and 22BPY in the corresponding conformation. Color codes are Au (gold), Ag (silver), N (blue), C (gray), and H (white).

Figure 4 compares the experimental and computational SERS spectra of 22BPY molecules adsorbed on the pure Au nano disc. The background arising from the Raman bands of glass was subtracted from experimental SERS for better comparison with DFT simulations. A vertex complex with one-metal-atom model (Fig. 4b) and three complexes (Figs. 4c-e) were used for 20-metal-atom model, one of which is a vertex complex (**V**) and other two were planar complexes (**P**) with the cis and trans conformers of 22BPY. Structural and electronic properties for M_{20} and 22BPY-M_{20} are summarized in ESI†. In the complex **V**, 22BPY binds to one of the vertex of pyramidal Au_{20} with the cis-conformation making two N-Au bonds. In the case of complex **P**, both the cis- and trans-conformations of 22PY are considered to be physically flatly adsorbed on one of the (111) facets of Au_{20}, The optimized structure shows that the cis-conformer binds to the surface lifting up one of the Au atom, as shown in the right of Fig. 3.

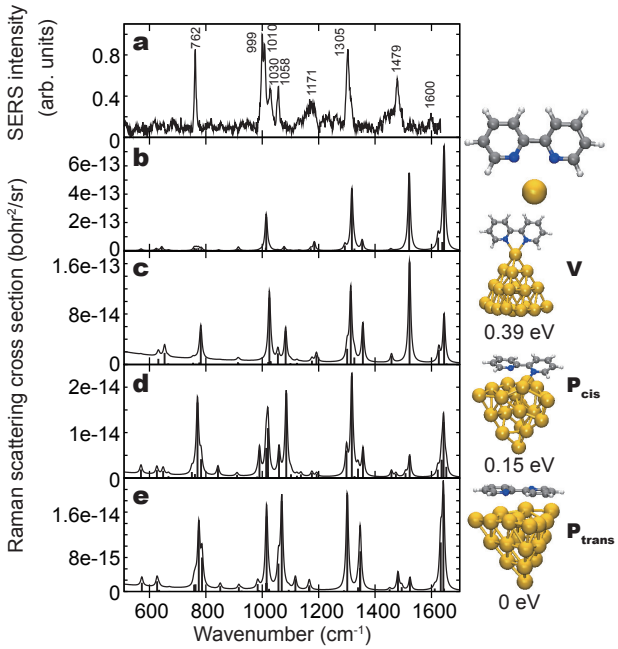

Figure 4: SERS spectra of 22BPY adsorbed on the Au. (a) Experimental and (b-e) computational results. Models used for numerical simulation are shown in the right along with the relative total energies for the Au_{20}-22BPY models.

Both the experimental and computational spectra show peaks around (1) 762 cm^{-1}, (2) 1000-1060 cm^{-1}, (3) 1180 cm^{-1}, (4) 1300 cm^{-1}, (5) 1480 cm^{-1}. Vibrational modes for these peaks are assigned in Table S4 where the vibrational modes are named according to ref. [D40] The assignment is carried out for the complex $\mathbf{P_{trans}}$ because the abundance ratio is over 99% against the complexes **V** and $\mathbf{P_{cis}}$ according to the Boltzmann distribution estimated using the total energy differences, as shown in the right to the computational models in Fig. 4. Peak positions in the Raman spectra vary only by $\sim$5 cm^{-1} depending on the structures considered, whereas the peak intensities vary more broadly.

A peak at 762 cm^{-1} in Fig. 4a, is reproduced for all the computational spectra. It is very weak for the one-metal-atom model (Fig. 4b). This peak is strong for the **P** conformations following the trend observed in experiments. For $\mathbf{P_{cis}}$ and $\mathbf{P_{trans}}$, this peak mainly consists of two vibrational modes. One is a C-H out-of-plane wagging mode,

i.e., the in phase collective C-H out-of-plane bending motion. In the case of benzene, this mode is Raman inactive because this mode does not change the polarizability. For both cis- and trans-22BPY, this mode becomes Raman active owing to the lower symmetry than benzene but still weak. In the present case, this peak is very weak for **V** complexes because the symmetry is not largely changed from the molecule itself. In the **P** conformations, this peak becomes intense because of the symmetry breaking for the wagging mode by contact of the 22BPY molecule with the metal surface from one side. The other mode corresponds to the shoulder found in the experiment (Fig. 4a) and is a combination of the ring deformation mode and C-H bending mode. This mode is observable for 22BPY-Au_{20} with **P** conformations, but very weak or almost negligible for 22BPY-Au_1 and 22BPY-Au_{20} (**V**) models. There are several peaks around 1000 cm^{-1}. They are assigned to the C-H bending and ring deformation modes; both symmetric and anti-symmetric modes exist. A strong peak around 1500 cm^{-1} is found for Au_1 and Au_{20}-V but weak for Au_{20}-P. This vibration is the inner-plane C-H bending and ring deformation modes. In the present experimental spectrum, peak around $1400 \sim 1600$ cm^{-1} is rather weak, in contrast to the computational result. In other reported spectra, this peak is generally strong [D25, D26] and the present discrepancy might be attributed to an experimental difficulty because around this region rather strong background signal is observed.

Figure 5 shows the spectra for the case of Ag. The S/N ratio is much higher for Ag than Au and the peak assignments are easier to assign. The wavenumber and the type of vibrational mode are very similar to the case of Au. Simulated Raman cross sections are also larger for Ag than for Au. In contrast to the Au, $\mathbf{P_{cis}}$ is not preferred in the case of Ag. The Raman signal around 800 cm^1 is very weak in previous study with Ag_{10} model [D26] even with co-planar adsorption geometry. The reason might be that in that study the dispersion interaction is not included and the distance between π rings plane and Ag(111) surface is too large to affect the symmetrical vibrational motion with respect to the molecular plane. In the present study the dispersion interaction is used and the distance can be closer than the Luo's study.

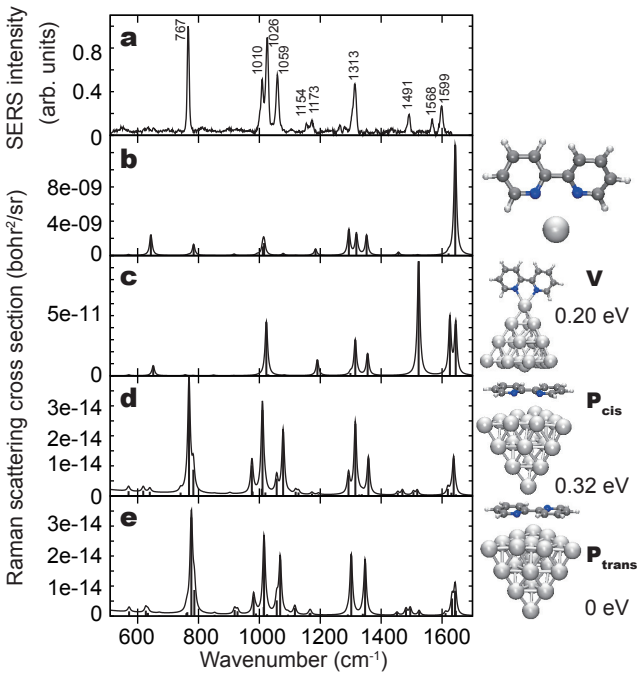

Figure 5: Calculated SERS spectra of 22BPY adsorbed on the Ag (same as Fig. 4 but for Ag).

For SERS using Au-Ag alloy, the model clusters are composed of Au_{10}-Ag_{10} following the experimental condition of co-mixing. As shown in Figure 1, six types of Au_{10}-Ag_{10} clusters were explored numerically in this study as a model system for the surface of alloy nanodiscs. Figure 6 shows the experimental and computational Raman spectra along with the optimized structures of 22BPY-$Au_{10}Ag_{10}$ complexes. The left, middle, and right column respectively shows the **V**, $\mathbf{P_{cis}}$, and $\mathbf{P_{trans}}$ conformations and the corresponding optimized structures are displayed in each row. Adsorptions in the planer conformations induces surface roughness. The N-atom prefers to bind with a silver atom rather to gold, leading to the structural distortions in the surface.

The peak intensities vary depending on the adsorption geometries, but spectral positions of the peaks are rather fixed. Around 800 cm^{-1} for **V**-complexes, the peaks are weak because of the symmetry. The same peaks of Fig. 6h and 6r are also weak perhaps because the substrate influence for the 22BPY is weak as compared to other

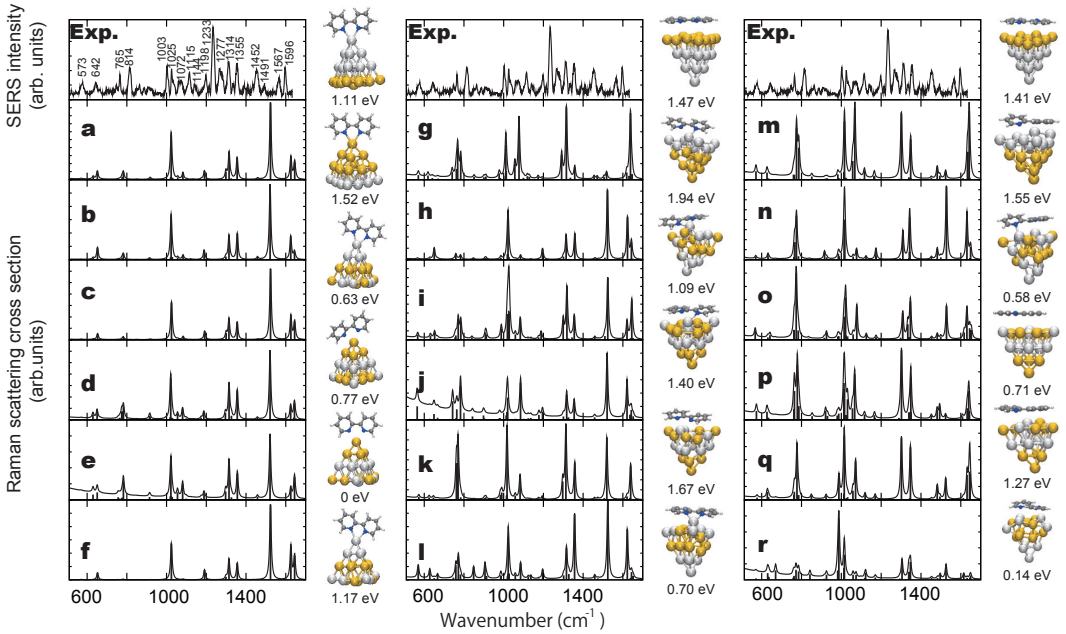

Figure 6: Calculated SERS spectra of 22BPY adsorbed on the Au-Ag alloy.

P-complexes. This trend is similar to the cases of Au_{20} and Ag_{20}.

Although many peaks match to the experiment, the most intense peak in experiment found at 1233 cm^{-1} is not reproduced in simulations. There are even no vibrational modes around this region. The discrepancy might arise from the isolated model system, different composition of surface, more rough surface, or a contamination by other molecules. Also the computed spectra have strong peak around 1500 cm^{1}. This peak can corresponds to the peak found at 1491 cm^{-1} in the experiment, although the peak intensity is very well accord presumably due to the low S/N ratio of the experimental spectrum.

Peak position can be red-shifted when I consider the anharmonicity. The anharmonic effect is usually included by multiplying a scaling factor to the peak position. The scaling factor applied in the previous study was 0.96. [D26] In the present case, however, if I universally apply the scaling factor the spectral shape can be inconsistent because the peaks around 800 cm^{-1} is already found at somewhat smaller wavenumber as compared to the experiment. Also, in the case for Au and Ag, the spectra are well reproduced

without considering the scaling factor.

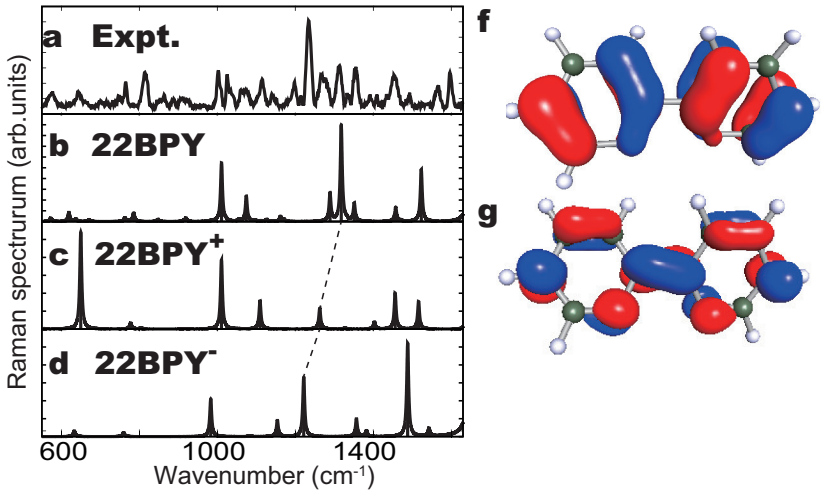

Figure 7: (a) Experimental SERS spectrum for 22BPY-Au/Ag alloy nanodiscs and computational Raman spectra of cis- (b) 22BPY, (c) 22BPY+, and (d) 22BPY-, (f) HOMO and (g) LUMO of 22BPY. Same vibrational modes that might be responsible for the peak shift in the alloy SERS of b-d are connected by the dotted line.

Generally, the peak shift can occur when bonds in a molecule are strengthen or weaken by charge transfer from substrate upon the adsorption. In my model complexes, however, we do not see such strong charge transfer and therefore peak shifts. In order to see the charge transfer effect, I here consider a cationic and anionic 22BPY. Figure 7 shows the Raman spectraand the HOMO/LUMO of 22BPY. The corresponding mode of 22BPY-Au and 22BPY-Ag are found at 1293 cm^{-1} and 1294 cm^{-1}, respectively. By looking at the vibrational mode, one can see that this vibration is due to the C-C stretching mode next to the N-atoms (C_1-C_2 and C_3-C_4). The HOMO and LUMO of 22BPY is bonding and anti-bonding character for these C-C bonds. In these charged states, the C-C bond weakens because the bond order decreases by removing bonding

electron for the cation and adding the anti-bonding electron for the anion. Upon charging and decrease of the C-C bond order, the peak position of **A** is red-shifted. The shift is largest for the anion and moderate for the cation. If the charge transfer occur from metal to 22BPY, LUMO of 22BPY will be occupied. This indicates that charge transfer can weaken the C-C bond and the vibrational mode shift to the lower energies. In the case of nanocluster, the ionization potential depends on the size, composition, structure, or charge.[D41] In the case of bulk surface, if the surface roughness become prominent, a local structure of the alloy might have locally different ability to donate an electron. This is suggested by the optimized 22BPY-$Au_{10}Ag_{10}$ complexes because adsorption onto alloyed surfaces distorts the surface morphology, see Fig. 3. In the cluster model, the number of electrons govern the ionization potential because of the quantum size effect of a delocalized valence electron over entire cluster. It is known as the superatom model, which is robust and geometry distortion weakly changes the ionization potential.[D42] Another possibility might be a charge transfer that can happen during SERS measurements from excited plasmons. [D43] The roughened surface, which could be easily occurring on the surface of Au-Ag alloy, could be responsible for increasing plasmon scattering.

4.4 Conclusion

SERS of bipyridyl on Au, Ag and Au-Ag alloy nanodisc arrays wastheoretically investigated. Quantum chemical study on the molecule adsorbed on 20-atom tetrahedral clusters clarifies that the molecule in trans-form prefers to co-planar adsorption on (111) face and most strong adsorption is found for pure Au surface. The adsorption on Au-Ag alloy surface can induce deformation and roughened the surface due to different affinity of the analyte molecue to Au and Ag, as well as different bonding intensity between metal atoms. One strong peak around 800 cm^{-1} can be reproduced with co-planar adsorption geometry by supporting one side of the analyte molecule breaking the symmetry of this vibrational mode to make this mode Raman active. For this adsorption, I believe that the dispersion interaction is mandatory.

Such alloy substrates can prove to be useful due to their higher sensitivity manifesting via the CE mechanism analyzed in this study. Precise mapping of surface nanoscale roughness and light intensity distribution can provide information where hot spots are formed and what light field components are created at the interface where analyte molecules bind. Further comparative studies between experimental SERS and DFT are greatly needed for reaching a quantitative match between experimental and theoretical descriptions which is vital for turning SERS into an analytical method.

Reference

[D1] J. Kneipp, H. Kneipp, and K. Kneipp, Chemical Society Reviews **37**, 1052 (2008).

[D2] P. G. Etchegoin and E. C. Le Ru, Physical Chemistry Chemical Physics **10**, 6079 (2008).

[D3] A. R. Bizzarri, International Journal of Nanomedicine , 2033 (2011).

[D4] R. S. Golightly, W. E. Doering, and M. J. Natan, ACS Nano **3**, 2859 (2009).

[D5] Y. Cui, R. S. Hegde, I. Y. Phang, H. K. Lee, and X. Y. Ling, Nanoscale **6**, 282 (2014).

[D6] K. Kneipp et al., Physical Review E **57**, R6281 (1998).

[D7] X.-M. Qian and S. M. Nie, Chemical Society Reviews **37**, 912 (2008).

[D8] S. M. Stranahan and K. A. Willets, Nano Letters **10**, 3777 (2010).

[D9] L. Morton, S.M. Silverstein, D.W. Jensen, Chem. Rev. **111**, 3962 (2011).

[D10] M. K. Schmidt, R. Esteban, F. Benz, J. J. Baumberg, and J. Aizpurua, Faraday Discussions **205**, 31 (2017).

[D11] M. K. Kinnan and G. Chumanov, The Journal of Physical Chemistry C **111**, 18010 (2007).

[D12] Y. Nishijima, Y. Hashimoto, L. Rosa, J. B. Khurgin, and S. Juodkazis, Advanced Optical Materials **2**, 382 (2014).

[D13] Y. Nishijima, J. B. Khurgin, L. Rosa, H. Fujiwara, and S. Juodkazis, ACS Photonics **1**, 1006 (2014).

[D14] S. Jayawardhana, L. Rosa, S. Juodkazis, and P. R. Stoddart, Scientific Reports **3**, 2335 (2013).

[D15] P. Reineck et al., ACS Nano **7**, 6636 (2013).

[D16] Y. Zheng et al., Journal of Materials Chemistry A **3**, 240 (2015).

[D17] J. R. Lombardi, R. L. Birke, T. Lu, and J. Xu, The Journal of Chemical Physics **84**, 4174 (1986).

[D18] C. M. Aikens and G. C. Schatz, J. Phys. Chem. A **110**, 13317 (2006).

[D19] C. Gong and M. S. Leite, ACS Photonics **3**, 507 (2016).

[D20] M. R. S. Dias, C. Gong, Z. A. Benson, and M. S. Leite, Advanced Optical Materials **6**, 1700830 (2018).

[D21] Y. Nishijima et al., Optics Express **25**, 24081 (2017).

[D22] Y. Hashimoto, G. Seniutinas, A. Balčytis, S. Juodkazis, and Y. Nishijima, Scientific Reports **6**, 25010 (2016).

[D23] C. Kaes, A. Katz, and M. W. Hosseini, Chemical Reviews **100**, 3553 (2000).

[D24] T. Dretschkow, D. Lampner, and T. Wandlowski, Journal of Electroanalytical Chemistry **458**, 121 (1998).

[D25] A. Brolo, Z. Jiang, and D. Irish, Journal of Electroanalytical Chemistry **547**, 163 (2003).

[D26] Z. Luo, B. H. Loo, X. Cao, A. Peng, and J. Yao, The Journal of Physical Chemistry C **116**, 2884 (2012).

[D27] M. Takenaka et al., Journal of Computational Chemistry **40**, 925 (2019).

[D28] C. Lee, W. Yang, and R. G. Parr, Physical Review B B **37**, 785 (1988).

[D29] A. D. Becke, The Journal of Chemical Physics **98**, 5648 (1993).

[D30] S. Grimme, J. Antony, S. Ehrlich, and H. Krieg, The Journal of Chemical Physics **132**, 154104 (2010).

[D31] K. Eichkorn, F. Weigend, O. Treutler, and R. Ahlrichs, Theoretical Chemistry Accounts: Theory, Computation, and Modeling (Theoretica Chimica Acta) **97**, 119 (1997).

[D32] A. Schäfer, H. Horn, and R. Ahlrichs, The Journal of Chemical Physics **97**, 2571 (1992).

[D33] TURBOMOLE V7.0 2015, a development of University of Karlsruhe and Forschungszentrum Karlsruhe GmbH, 1989-2007, TURBOMOLE GmbH, since 2007; available from http://www.turbomole.com.

[D34] R. Ahlrichs, M. Bär, M. Häser, H. Horn, and C. Kölmel, Chemical Physics Letters **162**, 165 (1989).

[D35] F. Furche and R. Ahlrichs, The Journal of Chemical Physics **117**, 7433 (2002).

[D36] D. Rappoport and F. Furche, The Journal of Chemical Physics **126**, 201104 (2007).

[D37] L. Hong et al., Computational and Theoretical Chemistry **993**, 36 (2012).

[D38] S. Heiles, A. J. Logsdail, R. Schäfer, and R. L. Johnston, Nanoscale **4**, 1109 (2012).

[D39] P. Pyykkö, Angewandte Chemie International Edition **43**, 4412 (2004).

[D40] M. Muniz-Miranda, E. Castellucci, N. Neto, and G. Sbrana, Spectrochimica Acta Part A: Molecular Spectroscopy **39**, 107 (1983).

[D41] W. A. de Heer, Reviews of Modern Physics **65**, 611 (1993).

[D42] P. Jena, The Journal of Physical Chemistry Letters **4**, 1432 (2013).

[D43] E. A. Sprague-Klein et al., Journal of the American Chemical Society **139**, 15212 (2017).

5 Near-field Raman

5.1 Introduction

The near field refers to electromagnetic field near a surface. Localization of the near field has been utilized in molecular spectroscopy and microscopy to achieve a spatial resolution beyond the diffraction limit of the propagating light. Recently, chemical reactions induced by near field have been studied.[E1, E2, E3, E4] Near-field vibrational spectroscopy using a plasmon field has been widely adopted as a surface-enhanced vibrational spectroscopy method. IR spectroscopy using a plasmonic metal nanostructure is called surface-enhanced infrared spectroscopy (SEIRAS).[E5] In the case of Raman effects, it is called surface-enhanced Raman spectroscopy (SERS).[E6] Notably, because of the localized nature of the near field, the induced molecular excitation can be non-dipolar, which is different from the case with propagating light (plane wave).[E7]

Among near-field Raman spectroscopy techniques, I focus on tip-enhanced Raman spectroscopy (TERS), a type of surface-enhanced vibrational spectroscopy using a metal tip.[E8, E9, E10] Localized surface plasmon resonance of a metal probe is accompanied by a strongly enhanced local electric field compared to the incident light. This local field induces dipole moment in a nearby molecule, and scattered light is detected as enhanced Raman signal. There are two main experimental approaches for TERS. In atomic force microscope (AFM)-TERS,[E11] the AFM probe is coated with a thin film of plasmonic metal (e.g., Au, Ag).[E12] The other is scanning tunneling microscope (STM)-TERS. In both techniques, an enhanced electric field is generated at the gap between the microprobe and the metal surface.[E13] The plasmonic field is not only strong but also spatially non-uniform at the molecular scale. Therefore, peaks of Raman-forbidden modes can be observed owing to the electric field gradient[E14] as is the case with SERS.[E15]

One of the advantages of TERS is high spatial resolution in the Raman spectra and imaging. By scanning the tip over a molecule, Raman spectrum can be obtained at each point, which allows one to map the Raman spectral intensities. A 15-nm resolution

with ultra-high vacuum (UHV)-TERS was reported in 2008.[E16] In a dry nitrogen environment at room temperature, a 1.7-nm imaging resolution was reported for carbon nanotubes using STM-TERS.[E17] Recently, sub-molecular scale resolution[E18] and molecular vibrational mode dependency have been reported.[E19] In those experiments, either the molecules are directly adsorbed onto the metal surface, and/or the distance between the molecule and the metal tip is small. In such conditions, chemical interaction between the metal tip or substrate and the molecule may be important for the peak enhancement, as in the case of SERS.

Theoretical methods have been developed to understand the atomic resolution of TERS mapping. Jensen et al. developed a discrete interaction model/quantum mechanics (DIM/QM) method to calculate single-molecule TERS imaging maps. The effect of metal atoms in the tip is accounted for by classical atomic polarizability, while the molecule is modeled by quantum chemistry.[E20] Those authors also showed the importance of electric field gradient in Raman spectra when the molecule was at the gap between the metal surface and the metal tip (modeled by a cluster). The dependence of the TERS signal of a single molecule on its vibrational modes was clarified. Recently, a locally integrated Raman polarizability density (LIRPD) method was proposed for understanding the mechanisms and selection rules of TERS.[E21] The method handles the Raman polarization density of the molecule and the near-field distribution with a low computational cost, and it can qualitatively reproduce computational results of the DIM/MM method. Luo et al. developed a computational method that considers the effect of spatially confined plasmons (SCPs) based on the gauge-invariant Hamiltonian, and reported that SCP localized in a few angstroms can achieve atomic-scale resolution.[E22, E23, E24, E25] Kupfer et al. investigated the quantum chemical effect for off- and on-resonance TERS of a naphthalocyanine molecule, and the tip was modelled by Ag atom/cluster. The excited states of the entire tip-molecule system was calculated by time-dependent density functional theory (TDDFT).[E26] The role of the charge-transfer state and intramolecular excitation state have been well studied for TERS imaging.

Conventional surface-enhanced spectroscopy is understood from both chemical and electromagnetic viewpoints. In recent experiments, the molecule can be decoupled from the surface and the tip by inserting an insulating NaCl thin film and positioning the STM tip away from the molecule, respectively. Such experiments have been performed to measure the molecule free from chemical effects.[E27] The insulator is inserted between the sample and substrate to decouple their electronic interaction. Recently, single-molecule STM-TERS using NaCl films was reported, and vibrational mode dependency was clearly observed.[E28] In that experiment, the energy of the incident light was tuned to the excited state, which has a transition dipole moment parallel to the substrate. Under this condition, signal enhancement by the electromagnetic field may become dominant. The electric field component parallel to the surface may play a role in the peak selectivity of the Raman spectrum, especially under the resonance condition.

Among these new experiments, I am interested in the intrinsic selection rule of a molecule excited by near field. I have previously studied the interaction between molecules and the near field using a multipolar Hamiltonian, which includes the infinite number of multipole interaction terms between the molecule and electric field. For application to surface-enhanced vibrational spectroscopy, a computational method for near-field IR was developed.[E29, E30] In the case of IR spectroscopy, one only needs to calculate the ground state of the molecule. However, Raman spectroscopy uses the scattering from molecules; therefore, the electronically excited states need to be calculated. Near-field electronic excitation was studied as a real-time electron dynamics of NC_6N with real-space real-time TDDFT.[E31] This method could be used to understand the new experiments because the spatial structure of the near field can be explicitly treated.

The current paper presents a computational method for Raman spectroscopy with non-uniform electric fields using real-time time-dependent density functional theory (RT)-TDDFT. The spatial distribution of the electric field is fully treated, and the peak intensity is calculated from the induced dipole moment. A method with RT-TDDFT has already been developed to compute Raman spectra under dipole approximation.[E32] It was shown that the dipole polarizability under electron resonance conditions, calculated

from the time propagation under linear perturbation conditions, is the same as that obtained using Jensen ' s polarizability method.[E33, E34] The merit of RT-TDDFT is the computational efficiency[E33] and ability to achieve massive parallelization when in combination with real space method.[E35] As an example, excited states of nanometer-scale gold clusters have been calculated with a massively parallel computation.[E36] Also, the current approach can calculate both the resonance and non-resonance Raman spectra by only changing the energy of the incident field.

5.2 Theory

The Raman signal is detected as scattered light generated from the induced dipole moment of a molecule.[E37] The intensity of the Raman spectra for the k-th normal mode I_k is proportional to the square of the derivative of the induced dipole moment by normal coordinale Q_k.

$$I_k \propto \left| \frac{\partial \boldsymbol{\mu}^{\mathrm{ind}}(\omega)}{\partial \boldsymbol{Q}_k} \right|^2 \tag{1}$$

where ω is the frequency of the incident light. This formula assumes that the observer is located far from the molecule, so that the higher multipole radiation can be neglected. Therefore, Eq. 1 may be used even when the molecule is irradiated by a complex electric field under typical experimental conditions. Meanwhile, the experimental conditions affect which component of the induced dipole moment produces the observed scattered light.

The frequency-dependent induced dipole moment $\mu^{\mathrm{ind}}(\omega)$ is calculated by Fourier transform of the time-dependent induced dipole moment μ^{ind}(t)

$$\boldsymbol{\mu}^{\mathrm{ind}}(\omega) = \int \boldsymbol{\mu}^{\mathrm{ind}}(t) e^{-i\omega t} dt \tag{2}$$

μ^{ind}(t) is derived from the time-dependent electron density.

$$\boldsymbol{\mu}^{\mathrm{ind}}(t) = \int \delta\rho(\boldsymbol{r}, t) \cdot \boldsymbol{r} d\boldsymbol{r} \tag{3}$$

$$\delta\rho(\boldsymbol{r}, t) = \rho(\boldsymbol{r}, t) - \rho(\boldsymbol{r}, 0) \tag{4}$$

where ρ is the electron density and $\delta\rho$ is its variation. The $\delta\rho$ induced by external fields can be obtained by solving the time-dependent Kohn–Sham equation as follows:

$$i\frac{\partial}{\partial t}\phi_i(\boldsymbol{r},t) = \left(-\frac{\nabla^2}{2} + V_{\mathrm{H}}(\boldsymbol{r},t) + V_{\mathrm{xc}}(\boldsymbol{r},t) + V_{\mathrm{ext}}(\boldsymbol{r},t)\right)\phi_i(\boldsymbol{r},t) \tag{5}$$

$$\rho(\boldsymbol{r},t) = \sum_{i=1}^{n} |\phi_i(\boldsymbol{r},t)|^2 \tag{6}$$

where ϕ_i is the Kohn-Sham orbital, V_{H} is the Hartree potential, V_{xc} is the exchange-correlation potential, and V_{ext} is the external potential. By using the external potential, which includes the interaction between the molecule and the non-uniform electric field, the induced dipole moment can be obtained. In this study, I used a multipolar Hamiltonian that considers all the multipolar interactions between the molecule and the external electric field. Then I will have the next interaction Hamiltonian.

$$V_{\mathrm{ext}}(\boldsymbol{r},t) = -\int \hat{\boldsymbol{P}}(\boldsymbol{r},t)\cdot\boldsymbol{E}(\boldsymbol{r},t)d\boldsymbol{r} \tag{7}$$

where $\hat{\boldsymbol{P}}$ is the electric polarization field, and its explicit form is:

$$\boldsymbol{P}(\boldsymbol{r}) = \sum_{\alpha} e_\alpha(\hat{\boldsymbol{q}}_\alpha - \boldsymbol{R})\int_0^1 d\lambda\delta[\boldsymbol{r} - \boldsymbol{R} - \lambda(\hat{\boldsymbol{q}}_\alpha - \boldsymbol{R})] \tag{8}$$

where e_α and $\hat{\boldsymbol{q}}_\alpha$ are respectively the charge and position operator of the αth electron in the molecule. The Taylor expansion of this electric polarization field gives multipoles such as dipoles, quadrupoles, octapoles, etc.

In sharp contrast to the dipole approximation aided by higher multipoles, here I use the above original form of the electric polarization field without any truncation. This means that all orders of the multipole are considered. For the DFT calculation, the multipolar potential is defined by the following formula.[E31]

$$V_{\mathrm{ext}}(\boldsymbol{r},t) = (\boldsymbol{r} - \boldsymbol{R})\cdot\boldsymbol{E}_{\mathrm{eff}}(\boldsymbol{r},t) \tag{9}$$

$$E_{\mathrm{eff}}(\boldsymbol{r},t) = \int_0^1 d\lambda\boldsymbol{E}\left[\boldsymbol{R} + \lambda(\boldsymbol{r} - \boldsymbol{R}), t\right] \tag{10}$$

where $\boldsymbol{R}$ is the center of mass of the molecule. The integration of λ comes from the definition of the electric polarization field. In Eq. 9, a spatially non-uniform electric

field obtained numerically by solving Maxwell ' s equations can be used as the external field. For example, an electric near-field around a silver nanoplate was used in my previous study to obtain near-field IR spectra.[E30]

Before going to the next chapter, I would like to mention on the multipolar expansion. We rely on the above mentioned framework, which begin by the Taylor expansion of charge density, while other way can be the expanding the non-uniform field itself.[E38] They give the same result. The expansion of the charge distribution includes the derivative on the Dirac ' s delta function. By integrating the Eq. 7 by parts, the derivative on the delta function moves to the electric field, and then the form will look the same. The use of the Taylor series of charge distribution for the interaction Hamiltonian can then leads to multipolar magnetic interactions in the full multipolar Hamiltonian (this is not included in my paper).[E39] For both frameworks, the first interaction is a point charge and scalar potential, and the next term is a dipole and electric field, and then quadrupole moment and field gradient, and so forth. The use of low-rank multipole interaction works for the slowly varying field. In the near-field case, however, the field has a very sharp intensity decrease, and the distribution of the electric field vectors is not uniform or even radially distributed, as shown in Fig. 2. For such cases, using all the multipolar interactions up to infinite orders (i.e., using Eq. 8) would be convenient compared to the adding higher-order multipoles one by one to the dipole interaction because the convergence with finite orders of multipole interactions is not guaranteed and then an infinite order of multipoles maybe necessary.

5.3 Computational details

5.3.1 Computational scheme

First, geometry optimization and normal mode analysis are performed for the molecule in the electronic ground state. Next, excited-state calculations are performed with the real-time propagation method. The time variation of the induced dipole moments is calculated for distorted geometries, where the coordinate of one atom is slightly displaced in each of the x, y, and z directions. Third, Fourier transformation is applied to the

induced dipole moment to obtain its counterpart in the frequency domain. Fourth, the derivatives of $\boldsymbol{\mu}^{\mathrm{ind}}$ with respect to the atomic Cartesian coordinates are calculated, and then transformed from Cartesian coordinates to normal coordinates using the transformation matrix L obtained by normal mode analysis. Finally, the Raman spectrum is obtained from the square of the absolute value of the normal coordinate derivatives of $\boldsymbol{\mu}^{\mathrm{ind}}$.

5.3.2 DFT and RT-TDDFT

All the main electronic structure calculations were performed with the real-time and real-space TDDFT program Octopus 9.2.[E40] The Perdew–Burke-Ernzerhof (PBE) density functional[E41, E42] and the SG15 Optimized Norm-Conserving Vanderbilt (ONCV) pseudo-potential[E43] were used. Instead of the more widely used basis sets, Octopus adopts a real-space grid technique. The computational space is made up by the superposition of spheres (radius: 7.0 Å) around the atoms. The mesh size of the computational space was 0.15 Å.

Normal mode analysis was performed using the finite difference method as implemented in Octopus. The default parametrization was used, in which the gradients are obtained when the atomic coordinates are shifted by 0.01 Bohr ($\sim$ 0.00529 Å).

For excited states, real-time electron dynamics calculations were performed. The time step of the real-time calculation was 0.0015 /eV ($\sim$ 0.99 as), and the total number of computational steps was 30000.

The absorption spectra were calculated using a δ pulse method.[E44] In this method, the ground state wavefunction perturbed by $e^{(i\delta \boldsymbol{k}\cdot\boldsymbol{r})}$ ($|\delta\boldsymbol{k}| = 0.01$ Å) was used as an initial wavefunction for real-time propagation with the molecular Hamiltonian (i.e., without any external fields).

For Raman spectra, the real-time calculation under dipole approximation was performed by applying the uniform electric field $\boldsymbol{E}$. The electric-field amplitude of uniform electric fields is set to 3.8×10^{-6} a.u. ($\sim 2.4 \times 10^{10}$ W/cm^2). For near-field excitation, the real-time propagation was performed under the external potential given by Eq. 9

generated by a point dipole, as described in the next chapter. I assume that these electric field oscillates at a frequency of ω. The envelope function ϕ is multiplied by the potential for numerical stabilization.

$$\phi(t) = \cos\left(\frac{\pi}{2} \cdot \frac{t - 3t_0}{t_0}\right) \tag{11}$$

A pulse duration of $t_0 = 620$ a.u. ($\sim$ 30 fs) is used in my calculation.

To analyze the electronic excitations, I calculated the Fourier transform of the electronic density as follows:

$$\delta\rho(\boldsymbol{r}, \omega) = \int \delta\rho(\boldsymbol{r}, t) e^{-i\omega t} dt \tag{12}$$

In the weak perturbation regime, the induced electron density is low (i.e., the mixing of excited states to the ground state wavefunction is very small). For such cases, the electron density difference can be approximated by the transition density.[E45, E46] The transition densities obtained in my method were compared with the TURBOMOLE results to assign the induced excited states.

5.3.3 Near field model

In this study, I calculated the TERS spectrum of benzene as an example. The near field around the metal tip is modeled by the near field of a point dipole expressed by Eq. 13.

$$\boldsymbol{E}^{\mathrm{nf}}(\boldsymbol{r}) = \frac{[3\boldsymbol{n}(\boldsymbol{n} \cdot \boldsymbol{\mu}) - \boldsymbol{\mu}]}{4\pi\epsilon_0 \boldsymbol{r}^3} \tag{13}$$

where $\boldsymbol{n}$ is the normalized coordinate vector, and $\boldsymbol{\mu}$ is the dipole moment. The effect of metal surface can be neglected as I focus on the experimental setup used in my previous paper[E28], in which the molecule is decoupled from the metal substrate by a NaCl thin film, as shown in Fig. 1(a).

From Fig. 1(b), the point dipole is located 5 Å above the benzene, and its strength is 1 Debye. The electric field distribution around the benzene is also shown in Fig. 2(a)–(d). The x and y components of the electric field have a ring-like intensity distribution, and the electric field vectors spread radially. The z component of the electric field radiates from the point dipole, and its intensity decreases with increasing distance from the dipole.

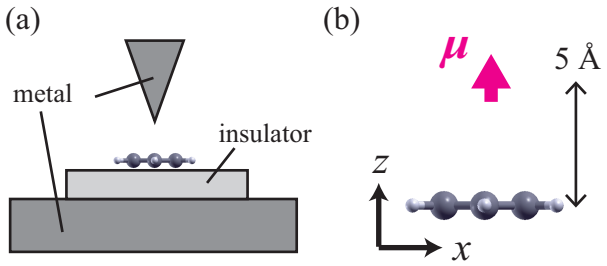

Figure 1: (a) Scheme of experimental setup, in which the insulator decouples the metal and benzene molecule. (b) The computational model, in which the point dipole is placed above the benzene and the origin is set at the center of benzene.

This electric field distribution is qualitatively consistent with that calculated using finite element method for the simulation of TERS experiment.[E47] The maximum intensity ratio of the x, y, and z components on the xy-plane is approximately 1:1:2.

In the previous experimental STM-TERS study[E28], the tip-molecule distance was set to 5.8 Å, in contrast to Apkarian ' s STM-TERS where the distance is smaller than 2Å.[E19] It was shown that with this larger tip-molecule distance, the intrinsic vibrational modes of the target molecule are rather unaffected, suggesting that chemical interactions (charge transfer and other perturbations) can be very weak or even ruled out. In the present model, the distance is not exactly the same as that experiment, but we believe that the present distance the chemical effect may not be dominant.

Numerical integration of Eq. 10 is done by

$$E_{\text{eff}}(\boldsymbol{r}, \boldsymbol{R}) = \sum_{i=0}^{M} \frac{1}{M} \boldsymbol{E}\left(\boldsymbol{R} + \frac{i}{M}\boldsymbol{r}\right) \tag{14}$$

where $\boldsymbol{R}$ is the center of gravity of the molecule. The points for calculating the electric field are independent of the grid for DFT calculations. In this study, I used $M = 100$. When I computed the Raman spectra for $M = 30$, 60, 100, 150, the peak distribution was almost unchanged and converged when the value of M became large. In this computational setup for benzene, the computational grids exist within 10 Å from the origin $\boldsymbol{R}$. Then, the largest step size is 0.33 Å when $M = 30$ and 0.1 Å when $M = 100$.

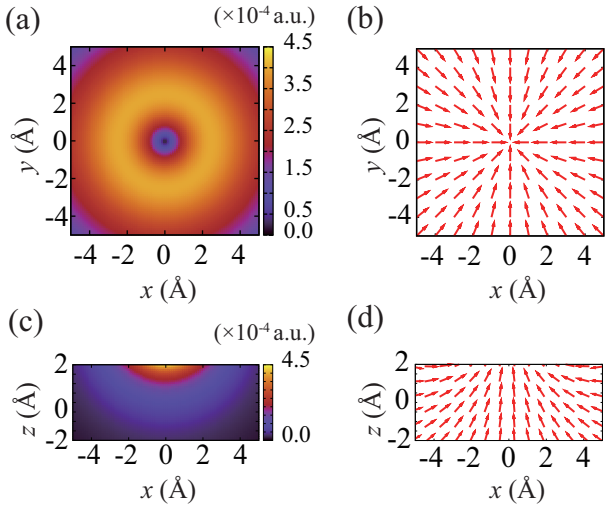

Figure 2: (a) Intensity map of $(E_x^2 + E_y^2)^{1/2}$ on the xy-plane. (b) Normalized electric field vectors on the xy-plane. (c) Intensity map of $(E_x^2 + E_z^2)^{1/2}$ on the xz-plane.(d) Normalized electric field vectors on the xz-plane.

5.3.4 Raman spectra

To obtain the Raman spectrum, I need the normal coordinate derivatives of the induced dipole moment $\boldsymbol{\mu}^{\mathrm{ind}}$, which is obtained from the Cartesian coordinate derivative of $\boldsymbol{\mu}^{\mathrm{ind}}$.

The normal coordinate derivative of the induced dipole moment in Eq. 1 is transformed from the Cartesian coordinate derivative by the transform matrix L, which is obtained by the normal mode analysis described above.

$$\frac{\partial \boldsymbol{\mu}^{\mathrm{ind}}(\omega)}{\partial Q_i} = \sum_{j=1}^{3N} L_{ji} \frac{\partial \boldsymbol{\mu}^{\mathrm{ind}}(\omega)}{\partial x_j} \tag{15}$$

where N is the number of atoms in the molecule, and x_j is the Cartesian displacement of atoms in the x, y, and z directions.

The Cartesian coordinate derivative in Eq. 15 is evaluated by

$$\frac{\partial \boldsymbol{\mu}^{ind}(\omega)}{\partial x_j} = \frac{\boldsymbol{\mu}^{ind}(\omega, x_j + \Delta x/2) - \boldsymbol{\mu}^{ind}(\omega, x_j - \Delta x/2)}{\Delta x} \tag{16}$$

where Δx is 0.04 Å in my calculation.

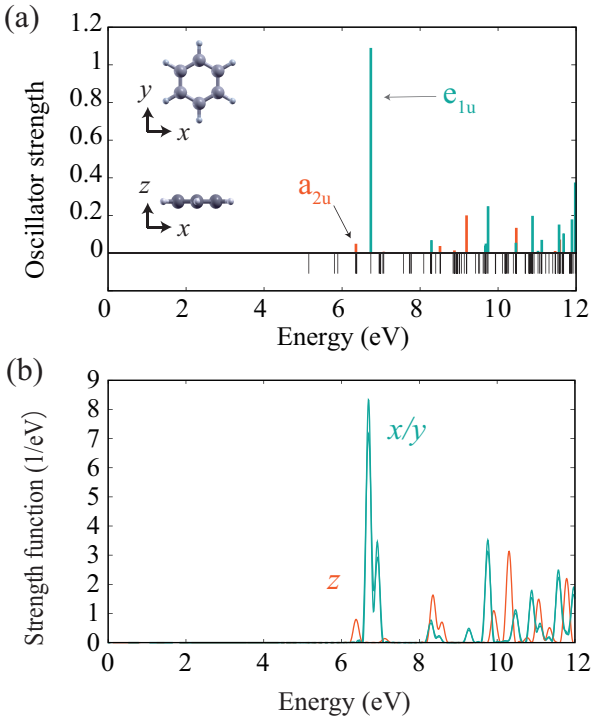

Figure 3: (a) Oscillator strength of benzene calculated by TURBOMOLE. The orange and green lines show peaks of the a_{2u} and e_{1u} excitations, respectively. The black lines under the spectrum indicate the positions of all excited states. (b) Strength function of Octopus from applying an impulsive force in either the x, y, or z directions. The peak area of the strength function corresponds to the oscillator strength.

5.4 Benchmark test

In order to check the accuracy of the present computational scheme and parametrization, I compared my calculated absorption spectra and off-resonance Raman spectra under the dipole approximation with those calculated by TURBOMOLE[E48] at the level of PBE/aug-cc-pVDZ[E49] under the resolution of the identity approximation. The use of large basis sets in TURBOMOLE is meant to account for the Rydberg character of the excited states, while the real-space grid techniques naturally describe the Rydberg character in Octopus with the present parametrizations.

Fig. 3 shows the absorption spectrum of benzene. The excited states allowed for x

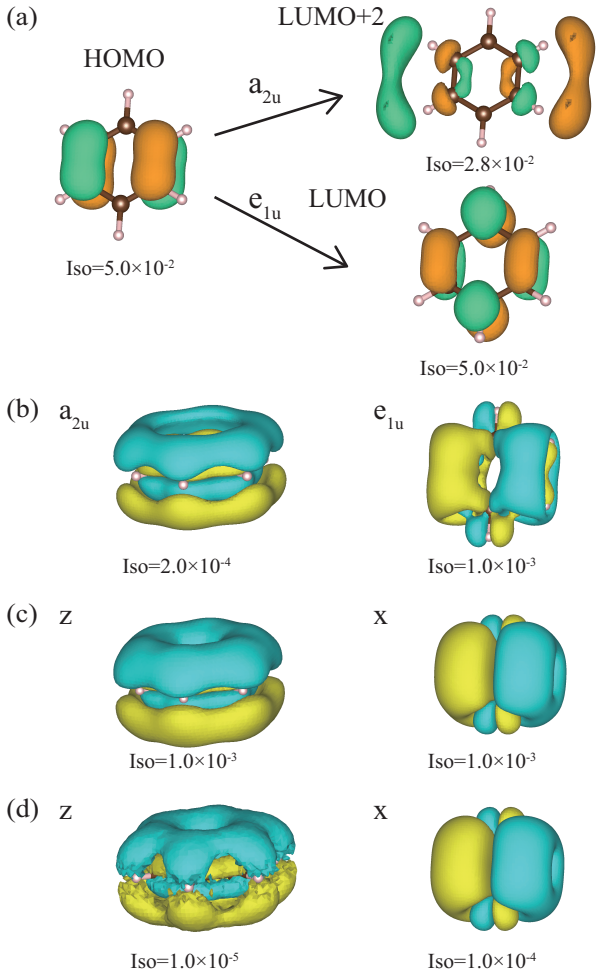

Figure 4: (a) Kohn-Sham orbitals obtained with TURBOMOLE concerning the lowest energy a_{2u} and e_{1u} excitations. These orbitals are doubly degenerate, and only one of them is shown for simplicity. (b) Transition densities of the lowest excited states of a_{2u} and e_{1u} symmetries obtained with TURBOMOLE. The yellow and blue surfaces represent positive and negative components, respectively. (c) Fourier-transformed electron density differences triggered by an impulsive force, obtained from RT-TDDFT calculations using Octopus. Left: $\omega = 6.36$ eV, force in the z direction. Right: $\omega = 6.70$ eV, force in the x direction. (d) Fourier-transformed electron density differences induced by a uniform electric field at the electronic excitation energies, obtained by RT-TDDFT calculations using Octopus. Left: $\omega = 6.36$ eV, electric field in the z direction. Right: $\omega = 6.70$ eV, electric field in the x direction.

and y are labeled as e_{1u} and for z are labeled as a_{2u}. The absorption spectra are almost quantitatively the same between the Octopus and TURBOMOLE calculations, while the absorption peak of e_{1u} is split for Octopus results. The calculations in Octopus do not use symmetry. Thus, x and y are not exactly the same in the real-space technique.

To assign the lowest-energy excited states, I compare the electron density difference obtained by Octopus with the transition density obtained by TURBOMOLE. The transition density is defined as the weighted sum of the product of occupied and virtual orbitals that form the excited state. The transition density is reported to correspond to the imaginary part of the Fourier-transformed electron density difference.[E46]

The Kohn-sham orbitals related to the lowest energy transitions for a_{2u} and e_{1u} are shown in Fig. 4(a) and the corresponding transition densities are shown in Fig. 4(b). These data are compared with the Fourier transform of the electron density difference obtained by Octopus in the real-time propagations with the δ pulse and uniform electric fields, as shown in Fig. 4c-d. Apparently, the shapes of transition densities in Figs.4(b)-(d) are almost the same as the Fourier transformed densities. By comparison, the lowest energy excited state for x/y is the $\pi - \pi^*$ transition, and that for z is termed as π to Rydberg σ^* transitions.[E50]

In the present calculation, I use generalized gradient approximation functional, which is known to underestimate the excitation energy, especially for extended states such as Rydberg states. To recover some of the deficiencies, a range separate or long-range corrected (LC) DFT would be required. As for the size of the basis sets, I used a real-space grid that can be considered to use very large basis sets and I consider that the spatial distribution of Rydberg states can be described fairly well. Also, Lorentzon et al., reported that the oscillator strength optained with CASSCF for this state is 0.052, which is very close to my TDDFT (TURBOMOLE) result (0.050).[E51] Based on these considerations, the present TDDFT calculations give qualitatively acceptable transition dipole moments and thus the Raman spectra. It is still very important, however, to clarify the use of TDDFT compared with highly accurate post-Hartree-Fock method, but this would require very efficient computational algorithm and this would be the

future challenge.

Figure 5 compares the off-resonance Raman spectra obtained with TURBOMOLE and my method. For comparison, the rotational average was taken for the off-resonance Raman spectra calculated with Octopus. Under this condition, the Raman signal of the ith mode is written as follows.[E52]

$$S_i = 45\left(\frac{\partial a}{\partial Q_i}\right)^2 + 7\left(\frac{\partial \gamma}{\partial Q_i}\right)^2 \tag{17}$$

$$a = \frac{1}{3}(\alpha_{xx} + \alpha_{yy} + \alpha_{zz}) \tag{18}$$

$$\gamma^2 = \frac{1}{2}[(\alpha_{xx} - \alpha_{yy})^2 + (\alpha_{yy} - \alpha_{zz})^2 + (\alpha_{zz} - \alpha_{xx})^2 + 6(\alpha_{xy}^2 + \alpha_{yz}^2 + \alpha_{zx}^2)] \tag{19}$$

where α is the polarizability tensor, a is the isotropic polarizability, and γ is the anisotropic polarizability. The off-resonance Raman spectra were obtained by using the dynamic polarizability at 3 eV by TURBOMOLE.[E53] In my approach, the ij component of the polarizability tensor α_{ij} can be calclated by

$$\alpha_{ij}(\omega) = \frac{\mu_i^{\mathrm{ind}}(\omega)}{E_j} \tag{20}$$

where E_j is the electric-field strength. For comparison, the normal Raman spectra under the dipole approximation are shown at the top of Fig. 5. The vertical axis represents the normalized Raman activity. As these off-resonance Raman spectra match very well, I consider the results of my calculations to be reliable.

5.5 Results and discussion

Here, I discuss the Raman spectra obtained using my approach, with a particular focus on the near-field excitations. The Raman spectra in the range of 0-1700 and 2700-3300 cm^{-1} are shown in Fig. 6, along with the corresponding vibrational modes. The normal Raman spectra are the same as those shown in Fig. 5b, but convoluted with the Lorentz function. For the near-field Raman spectra, the off-resonance and on-resonance conditions were considered. The near-field frequency of 3.0 eV was used for the off-resonance condition, and 6.36 and 6.70 eV for the on-resonance conditions. Compared

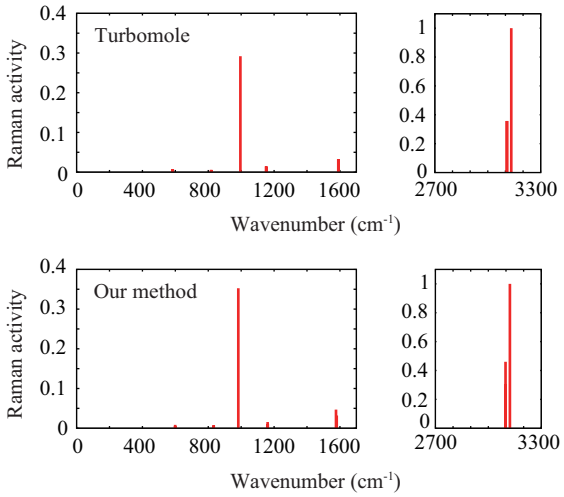

Figure 5: Normalized Raman activity of benzene calculated by TURBOMOLE and my method.

with the peak intensities of off-resonance Raman, those of on-resonance Raman at 6.36 and 6.70 eV are enhanced by about 100 times. In addition, the two on-resonance Raman spectra show different peak distributions. The x, y, and z contributions to $|\frac{\partial \boldsymbol{\mu}^{\mathrm{ind}}(\omega)}{\partial \boldsymbol{Q}_k}|^2$ are separately shown in Fig. 7 for analysis.

5.5.1 Off-resonance Raman

The peak selectivity under the off-resonance condition in Fig. 6(c) and (d) is explained by molecular vibrational symmetry and spatial structure of the near field.

Let us first focus on the Raman-forbidden modes in far-field Raman, which become active in near-field Raman. The vibrational mode **b** shown in Fig. 6 is Raman-forbidden because the normal coordinate derivative of the dipole polarizability is zero at the equilibrium structure. However, this mode is active and shows a peak in the near-field Raman spectra (Figs. 6(c) and (g)). From the decomposition in Fig. 7(a), this peak originates from the z component since the near field is not uniform, as shown in Fig. 8(a). In this condition, the normal coordinate derivative of the electric field and thus the induced dipole moment become nonzero at the equilibrium structure, $Q = 0$. The

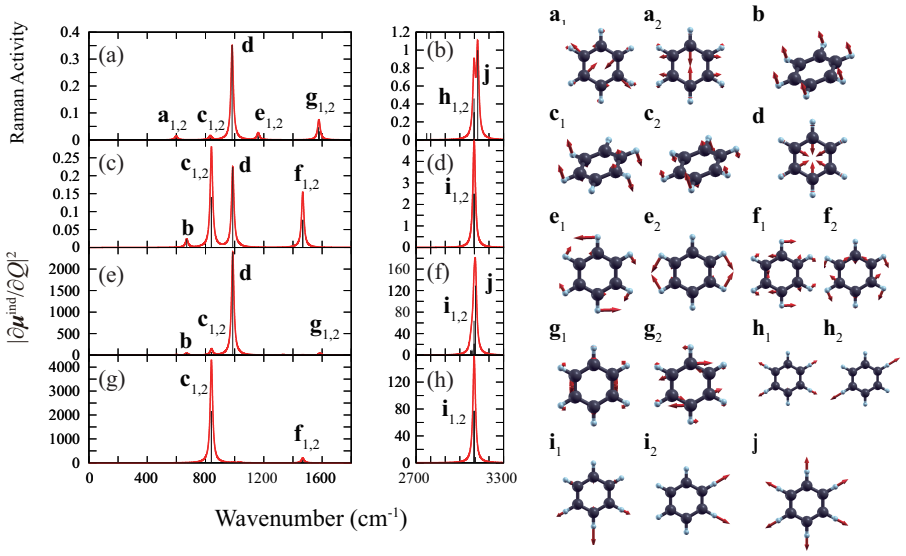

Figure 6: (a-b) Normalized far-field Raman activity of benzene. Near-field Raman spectra of benzene at the (c–d) off-resonance frequency condition (3.00 eV) and on-resonance conditions of (e–f) 6.36 eV and (g–h) 6.70 eV. The vibration modes labeled in the spectra are shown on the right.

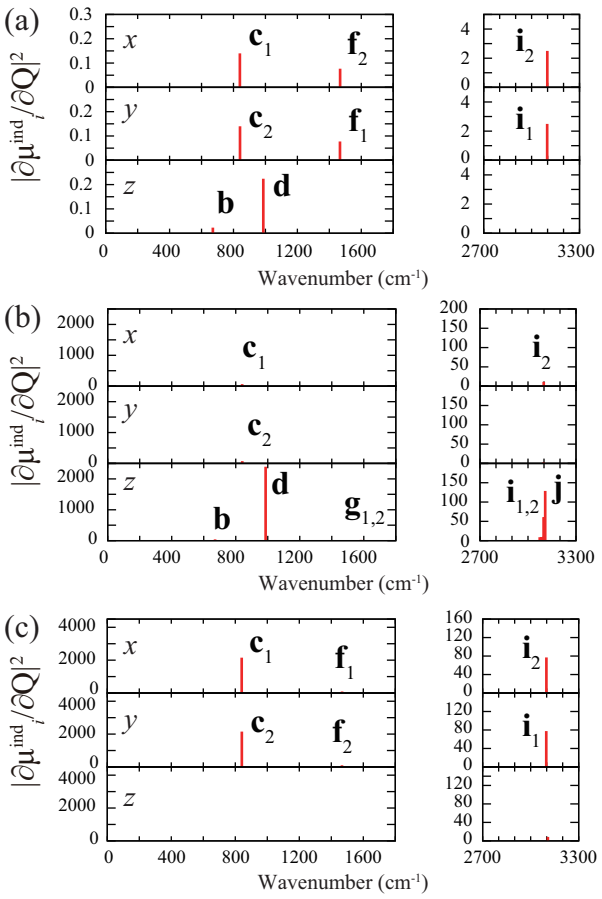

Figure 7: Decompositions of the near-field Raman activities shown in Fig. 6(c-h). The x, y, and z components of $|\frac{\partial \boldsymbol{\mu}^{ind}(\omega)}{\partial \boldsymbol{Q}_k}|^2$ with near-field frequencies at (a) 3.00 eV (off-resonance), (b)6.36 eV (a_{2u} resonance) and (c) 6.70 eV (e_{1u} resonance). The peak labels are the same as in Fig. 6.

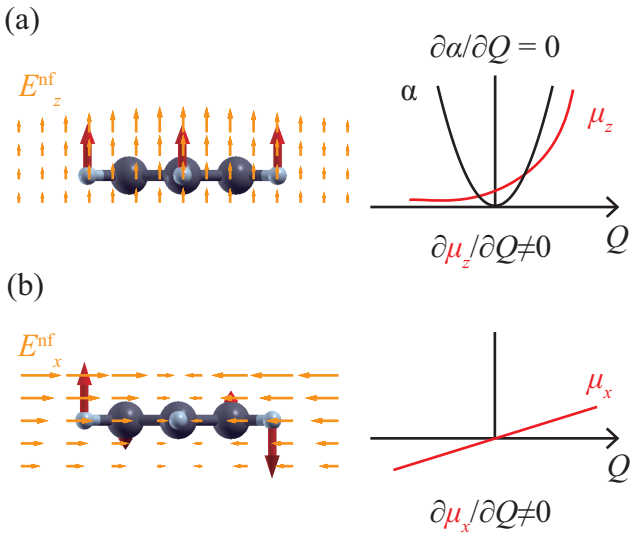

Figure 8: (a) The scheme of vibrational mode **b** and the E_z^{nf}, as well as the change of polarizability (black curve) and induced dipole moment (red curve) as a function of the normal coordinate. (b) The same for mode $\mathbf{c}_1$ and E_x^{nf}.

in-plane modes **f** and **i** are forbidden for the same reason as for mode **b** in the far-field Raman spectra. These modes also become active in near-field Raman, because E_x^{nf} and E_y^{nf} are non-uniform, which causes the normal coordinate derivative of the induced dipole moment to be nonzero at the equilibrium structure. In the near-field excitation, the induced dipole moment depends on the coupling between the higher-order polarizability and higher-order derivative of the electric field, as shown in Eq. (21).

$$\mu_i^{\mathrm{ind}} = \sum_j \alpha_{ij} E_j + \sum_{j,k} \frac{1}{3} A_{ijk} \frac{\partial E_j}{\partial k} + \ldots \tag{21}$$

In the SERS study on the gradient-induced breaking of the selection rule,[E15, E54, E55] quadrupole interaction was considered to explain the missing Raman peaks under the dipole approximation. Again, all these multipole interactions are included in my current calculation.

Next, we discuss the vibrational modes that are active in both far- and near-field Raman but with different origins. In far-field Raman, the peak $\mathbf{c}_1$ consists of xz and yz components in the polarizability derivative tensor. Therefore, all the directions of

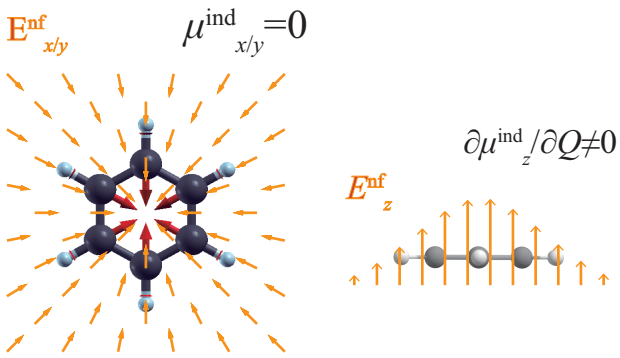

Figure 9: Schematic top and side views of the vibrational mode **d** and the near field.

$\boldsymbol{\mu}^{\mathrm{ind}}$ are concerned. On the other hand, in near-field Raman only μ_x^{ind} is concerned, as shown in Fig. 7(a). The motion of H atoms in the $\mathbf{c}_1$ mode is anti-symmetric in the z direction, as shown in Fig. 8(b). Together with the near-field distribution in Fig. 8(b), the direction of induced dipole moment is inverted by the $\mathbf{c}_1$ vibration, and thus $\partial\mu_x^{\mathrm{ind}}/\partial Q$ is nonzero. The same explanation holds for $\mathbf{c}_2$ mode and E_y^{nf}. The difference in the origin is prominent for peak **d**. This is the breathing mode of the carbon ring. In far-field Raman, the peak is derived from the xx and yy components of the polarizability. In near-field Raman, the E_x^{nf} and E_y^{nf} are distributed radially and cannot induce dipole moment within the xy-plane, as shown in Fig. 9. Thus, $\mu_{x/y}^{\mathrm{ind}}$ does not contribute to peak **d**. In near-field Raman, peak **d** comes from μ_z^{ind} since E_z^{nf} is non-unform, as shown in Fig. 9. These things are clearly shown in Fig. 7(a).

Finally, I discuss the peaks that are present in far-field Raman spectra but absent in the near-field Raman spectra, namely modes $\mathbf{a}_{1,2}$, $\mathbf{e}_{1,2}$, $\mathbf{g}_{1,2}$, $\mathbf{h}_{1,2}$, and **j**. Except for **j**, all these vibrational modes belong to the $\mathrm{E}_{2\mathrm{g}}$ symmetry. In the far-field spectra, contributions to these Raman signals come from the xx-yy and xy components of the polarizability derivative tensors, whereas the contributions from zz, xz, and yz are zero. According to my method, the signal consists of μ_x^{ind} and μ_y^{ind}. The present near field is radially distributed in the xy-plane, and therefore these contributions are zero. Although the near field is non-uniform in the z direction, the contribution from μ_z^{ind} still seems to

be very weak. As for mode **j**, its far-field Raman signal consists of μ_x^{ind} and μ_y^{ind}, while its near-field Raman signal consists of μ_z^{ind} as in mode **d**. However, compared to mode **d**, it seems that C-H stretching has little effect on the induced dipole, and the peak intensity is very weak. In short, the "missing" peaks in the near-field Raman are not forbidden but merely very weak, because the contributing components change between far-field and near-field illuminations.

5.5.2 On-resonance Raman

Compared to off-resonance near-field Raman, one more thing should be considered in resonance near-field Raman to understand the selection rule, namely the nature of the excited electronic state involved. Here, I applied the near field at the frequencies of 6.36 and 6.70 eV, which are the excitation energies of the a_{2u} and e_{1u} excited states, respectively. The Raman spectra shown in Fig. 6(e-h) are clearly different from the off-resonance ones. Furthermore, these spectra clearly depend on the frequency of the near field, suggesting that the involved excited electronic states are different. Figures 6(e-f) are spectra obtained with the near field at 6.36 eV, which can excite the lowest a_{2u} excited state. On the other hand, the spectra in Fig. 6(g-h) are obtained with the near field at 6.70 eV, and they are resonance Raman due to a vibronic coupling. At the equilibrium geometry, the molecule has D_{6h} symmetry, and the near field in the xy-plane is radially distributed. Therefore, the e_{1u} ($\pi - \pi^*$) state cannot be excited by the near field. When the molecule vibrates, however, the symmetry decreases, and the $\pi - \pi^*$ transition can be occured.

Let us first discuss the near-field Raman at the frequency of 6.36 eV. The corresponding electron density difference and Fourier transform of the induced dipole moment are shown in Fig. 10(a) and (c). Comparing them to Figs. 3 and 4, the lowest energy a_{2u} excited state seems to be excited. The asymmetry above and below the benzene ring plane originates from the inhomogeneous near field intensity, as the field distribution becomes wider away from the tip, as shown in Fig. 2(d). In this resonant condition, peak **d** is the strongest. This peak arises from μ_z^{ind} instead of $\mu_{x/y}^{\mathrm{ind}}$, for the same reason as in

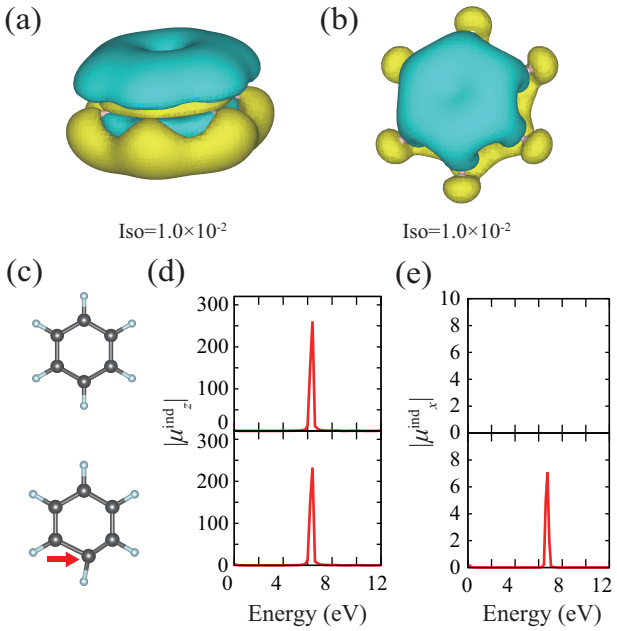

Figure 10: Fourier-transformed electron density differences for near-field excitations at (a) 6.36 eV and (b) 6.70 eV. (c) Benzene at the equilibrium structure and one of its distorted structures. The displaced C atom is indicated by the red arrow, and its displacement is exaggerated for visibility. The Fourier-transformed induced dipole moments of μ_z^{ind} and μ_x^{ind} obtained by near-field excitations at (d) 6.36 eV and (e) 6.70 eV, respectively, for the equilibrium (top) and distorted (bottom) structures.

the off-resonance condition (discussed above). In resonance Raman, molecular orbitals concerning the chosen excited state affect the peak selectivity. When the spatial overlap between the molecular orbitals and vibrational mode is large, the change in the induced dipole may also be large, giving rise to a large Raman signal. Under the near field at 6.36 eV, the peak **d** is large. From the decomposition analysis shown in Fig. 7, $\mu_z^{\rm ind}$ is the main contributor. Since the transition moment is also in the z-direction, the peak **d** is enhanced as in the case of off-resonance Raman discussed above. Mode **j** appears in the spectrum, but it is very weak in the off-resonance condition as discussed above. In the resonance condition, the orbitals involved in the excitation are extended to the C–H bonding orbitals, as shown in Fig. 10. The change in the induced dipole moment along this vibration becomes large, which enhances the Raman signal.

Next, I discuss the near-field Raman at 6.70 eV, shown in Figs. 6(g-h). Comparing the induced electron density difference at the equilibrium geometry (Fig. 10(b)) to that shown in Fig. 4, this excitation is apparently not the $\pi - \pi^*$ transition. However, when the molecule has a distorted structure (one of the atomic coordinates is shifted), the $\pi - \pi^*$ transition is excited, as shown in Fig. 10(d). Since this could be a vibronic effect, I will call it vibronic resonance Raman for the near field. Let me focus on the peak selectivity, where modes **c**, **f**, and **i** are active, although the latter two are very weak. Along the vibrational coordinate in the near field, these three modes can reverse the sign of the dipole moment in the xy-plane at the equilibrium geometry ($Q = 0$), while modes **b**, **d**, **h**, and **j** cannot. Therefore, modes **c**, **f**, and **i** are active in near-field Raman, although the dipole moment changes for the two in-plane modes (**f** and **i**) are very small compared to the out-of-plane mode **c**.

These results show that Raman spectra depend on the resonance condition, in particular the nature of the electronic transitions involved in resonance Raman. The present study considered the benzene molecule with high symmetry, but these discussions are also applicable to other molecules. The results here demonstrate that the present approach, which explicitly uses the full spatial structure of the electric field, facilitates understanding of the selection rule for near-field Raman.

Let me discuss my method comparing with Barone's formulation for resonance Raman with uniform light[E56] and Luo ' s generalization for localized light.[E57] Both of these formulations share the same discussion for vibrational states, while electronic transitions are different.

My protocol is rooted in the Jensen ' s polarizability method.[E34] Luber et al., demonstrated that this method can efficiently provide resonance Raman spectra for a uniform electric field excitation.[E33] The initial state is the ground states for both the electronic and vibrational states, and the final state is the first vibrational excited state in the electronic ground state. Only the fundamental peaks are considered. I do not explicitly consider the vibrational wavefunctions. my model corresponds to the situation where the electronic ground and excited states share the same equilibrium geometry and the harmonic potential. This is not a bad assumption because the optimized structure of the Rydberg state considered is almost the same to that of the ground state, where the Franck-Condon factor for the vibrational ground states (0-0 transition; $\langle v_0' \rangle \, v_0$) is larger than 0.99 and 0.94 for excitation with the electric field whose direction is in-plane and out-of-plane. The calculation of the FC factor is done with ezSpectrum 3.0.[E58].

Under these conditions, the intermediate states should be vibrational ground or first excited states, otherwise the integral is zero. The FC term is zero since if the intermediate state is $|v_0'\rangle$ then the integral with the final state $|v_1\rangle$ vanishes.[E59] In turn, if the intermediate state is $|v_1'\rangle$ then the integral with the initial state $|v_0\rangle$ vanishes. In the similar manner, the 4th term of Barone ' s eq. 10[E56] vanishes. The second and third terms can be survived with $\langle v_1|Q|v_0'\rangle \, \langle v_0'\rangle \, v_0$ and $\langle v_1\rangle \, v_1' \langle v_1'|Q|v_0\rangle$, respectively. Thus, these two terms can be present in my calculations.

The present Rydberg state accidentally has the similar equilibrium geometry to the ground state, allowing me to neglect the FC term. If this is not the case, one should explicitly consider the vibrational wavefunctions.

It should be worth mentioning that in my calculation the resonance electronic state is excited for distorted geometries, that excitation is forbidden for the pristine D6h structure. This should be related to the vibronic coupling, probably to Jahn-Teller

effect and I am currently cannot state that this is related to the HT effect, because the HT effect refers to the coupling between excited states, not between a virtual state and an excited state. Therefore I did not try to use the term “ HT “ but just “ vibronic ”. This should be studied in detail in the future.

As for the Cartesian displacements of 0.04 Å. This value is chosen for the numerical differentiation, but this displacement surely triggers the excitation to the excited state that is forbidden for the pristine D6h geometry and can have substantial effect on the resonance Raman spectrum.

5.5.3 Dependence on tip position

Near-field Raman spectroscopy, in particular STM-TERS, has been used to map molecular vibrations and studied theoretically.[E1, E19, E28, E26] I also reported resonance STM-TERS imaging experiments, but the molecule was decoupled from the metal surface and the STM tip. This is unlike the previous studies, in which the molecule is directly placed on a metal surface and the distance between the molecule and STM tip is very close, as discussed in the Introduction. Now, I calculate the tip position dependence of the Raman peaks for the off-resonance (3.0 eV) and two on-resonance (6.36 and 6.70 eV) conditions discussed above. Fig. 11 shows the position of the tip (i.e., the point dipole). Nine points were chosen for the Raman spectra calculations. The distance between adjacent points is 1 Å. The angle between the lines connecting A-E and A-I is 30°. I chose the same vibrational modes previously reported by Jensen et al., especially for discussing the field gradient effects.[E20, E21]

Fig. 12 shows the peak intensities and their decompositions for vibrational modes **b**, $\mathbf{c}_1$, $\mathbf{c}_2$and **j** as a function of the tip position under the off-resonance condition (3.0 eV). A dependence on the vibrational mode can be observed. The peak intensity for mode $\mathbf{c}_1$ decreases as the tip moves away from the molecular center, while mode **j** shows the opposite trend. The trend for mode **b** and $\mathbf{c}_2$ is intermediate between those of modes $\mathbf{c}_1$ and **j**.

The peak intensity of mode **b** is maximum at points B and F on each line. The main

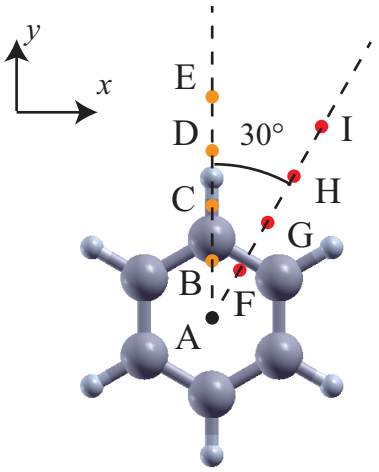

Figure 11: Positions of the dipole moment for calculating tip position dependence.

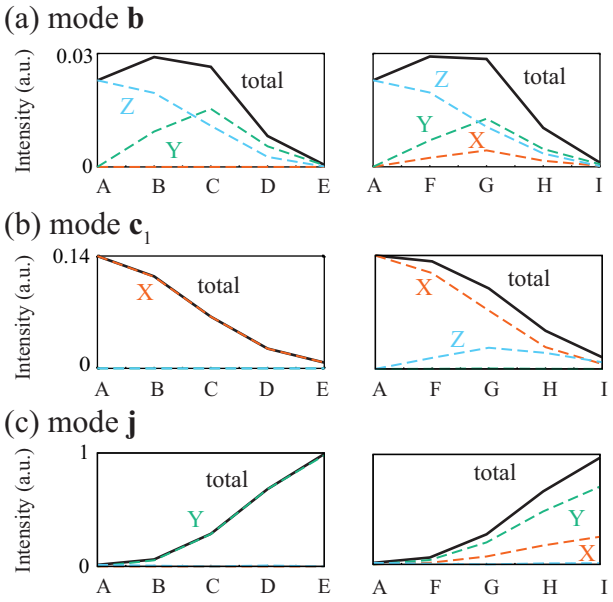

Figure 12: Raman intensity at each tip position, and the component of $\partial\boldsymbol{\mu}/\partial\boldsymbol{Q}$ at non-resonance condition (3.00 eV). The letters X, Y, and Z in the figure represent μ_x^{ind}, μ_y^{ind}, and μ_z^{ind}, respectively.

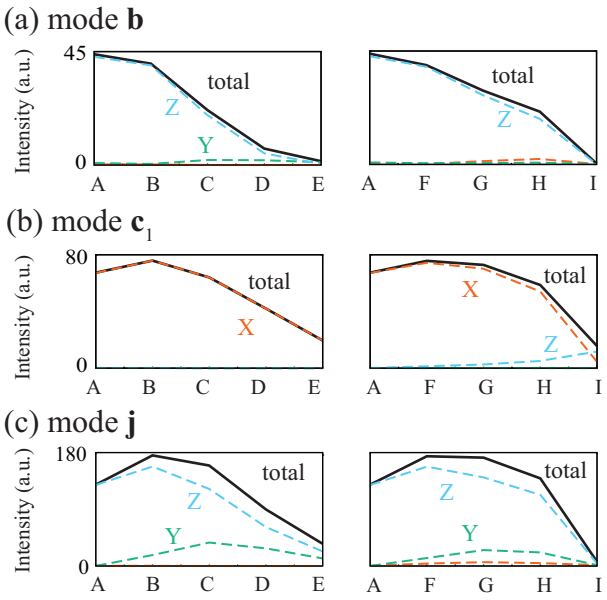

Figure 13: Raman intensity at each tip position and the component of $\partial\mu/\partial Q$ at resonance condition (6.36 eV).

contributors are μ_z^{ind} and μ_y^{ind}. The z component of the peak monotonically decreases, while the y component has a maximum at point C. When the tip is located at C, E_x^{nf} is symmetric and thus $\mu_x^{\mathrm{ind}} = 0$, whereas E_y^{nf} is asymmetric and thus $\mu_y^{\mathrm{ind}} \neq 0$. As the tip moves further to point E, the near-field itself becomes weak and therefore the peak intensity decreases. This is why $\partial\mu_y^{\mathrm{ind}}/\partial Q$ has a maximum at point C. Along line A-I, E_x^{nf} is also asymmetric, and thus μ_x^{ind} contributes to the peak intensity. The monotonic decrease in the contribution from μ_z^{ind} can be explained as follows. When the tip is at the molecular center, all the atoms can contribute to the induced dipole moment. On the other hand, when the tip is away from the center, atoms far from the tip contribute less, and therefore the peak intensity decreases.

The peak of mode $\mathbf{c}_1$ in Fig. 12(b) is exclusively composed of μ_x^{ind} on the line A-E. E_x^{nf} is symmetric along this line, and the contribution from μ_x^{ind} is shown in Fig. 8(b). When the tip is away from the molecular center, the electric field becomes weaker and the peak decreases monotonically. The z component also appears on line A-I. In mode

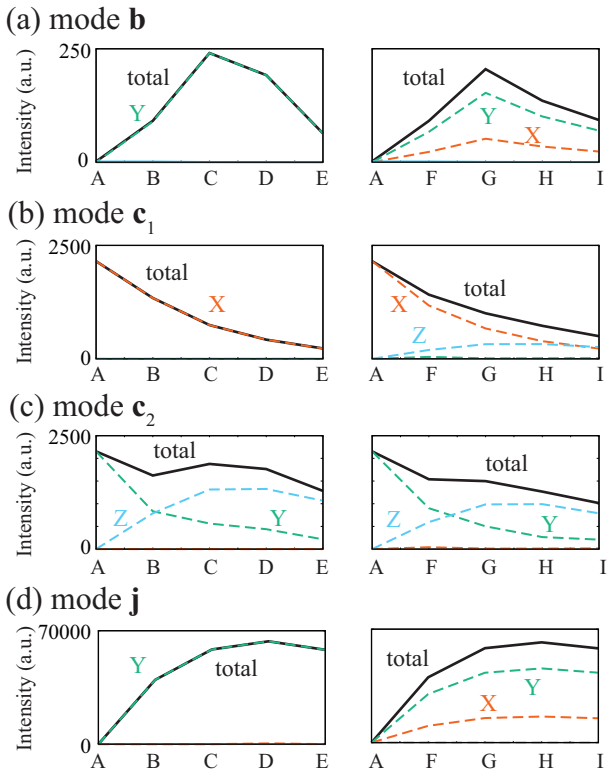

Figure 14: Raman intensity at each position, and the component of $\partial\mu/\partial Q$ at resonance condition (6.70 eV).

$\mathbf{c}_1$ (Fig. 6), most of the motion occurs in four hydrogen atoms. Because the tip position of G is closest to these hydrogen atoms, there is a large induced dipole moment in the z direction, which makes the largest contribution to peak intensity.

The peak of mode $\mathbf{c}_2$ is composed of μ_y^{ind} and μ_z^{ind}. The contribution from μ_y^{ind} monotonically decreases for the same reason as the contribution from μ_z^{ind} of mode **b**. The z component is maximum at points C and G on each line because most of the motion occurs in four atoms on y-axis in mode $\mathbf{c}_2$.

Mode **j** is the in-plane C-H stretching. When the tip is above the center of the molecule, this mode is not Raman active, while it is active in far-field Raman spectroscopy. As the tip moves away from the center of the molecule, the electric field approaches the far field, and thus the peak intensity monotonically increases.

Fig. 13 shows the Raman spectra at 6.36 eV. For mode **b**, the same discussion given above for off-resonance Raman holds. However, because the excitation is in the z direction, the largest contribution comes from μ_z^{ind} and very little comes from the x and y components. Mode $\mathbf{c}_1$ consists mostly of μ_x^{ind} as in the case of off-resonance Raman, but in the resonance condition the maxima are found at points B and F. This is likely because the amount of the induced dipole moment is larger when the tip approaches above the ring edge, where the electron density is larger than that inside the ring. In my method, the amount of excited state induced depends on the field intensity and its spatial variation. For mode $\mathbf{c}_2$, the z component monotonically increases on line A-E. The excited state is Rydberg π - σ^*, and thus the contribution from μ_z^{ind} may become large on the outside of the benzene ring. Mode **j** mostly consists of μ_z^{ind} at A, as discussed in Section VB. The maxima are found at B and F for the same reason as for mode $\mathbf{c}_1$.

Fig. 14 shows the Raman spectra at 6.70 eV. The behavior is mostly the same as the off-resonance case shown in Fig. 12. The main difference is that the excited state is $\pi - \pi^*$ (within the xy-plane), and thus the x and y components are dominant instead of the z component. In mode $\mathbf{c}_2$, the contribution from μ_z^{ind} is as large as μ_y^{ind}. Mode $\mathbf{c}_2$ belongs to $\mathrm{E}_{1\mathrm{g}}$ symmetry. In far-field spectra, the peak comes from the yz component of the polarizability derivative tensor. Therefore, as the tip moves away from the center

of the molecule, E_y^{nf} approaches the far field, and the contribution of μ_z^{ind} increases. In mode **j**, the intensity decreases when the tip is far away from the molecule. It can be understood that the amount of excited states becomes small when the tip is distant from the molecule. The decay would be faster for resonance Raman than for off-resonance Raman.

5.5.4 Mapping

Fig. 15 shows the map for these spectra. I have prepared the 2D images for the modes discussed in tip-position-dependencies. The images show vibrational mode dependencies as obtained via the linear response theory methods.[E20, E60] The simulated off-resonance Raman images show vibrational modes dependence as theoretically predicted[E57, E20] and later experimentally confirmed.[E19, E61] As modes **b** and **j** are C_6-symmetric, the map also has the same symmetry, but the bright positions are different. Mode $\mathbf{c}_1$ and $\mathbf{c}_2$ are lower symmetry than C_6, and thus the image also shows bright points different from modes **b** and **j**.

Our model is based on my previous study,[E28] in which E_x and E_y are also important in addition to E_z. The STM-TERS images obtained theoretically differ from those of previous studies.[E54, E20, E21] It is worth mentioning that Jensen et al. also indicated that the distance between the molecule and tip can significantly affect the TERS image, i.e., the relative peak intensities.[E21]

5.6 Conclusions

Here I propose a theoretical method for modelling near-field Raman in the regime beyond the dipole approximation. This method is based on the multipolar Hamiltonian, which can account for the full spatial distribution of the electric field. The method is well suited to my recent STM-TERS experiment that studied the intrinsic molecular properties. The electronic structure calculations are performed under the framework of real-time time-dependent density functional theory, which allows us to treat on- and off-resonance Raman on the same footing. The method was applied to the on- and off-resonance TERS

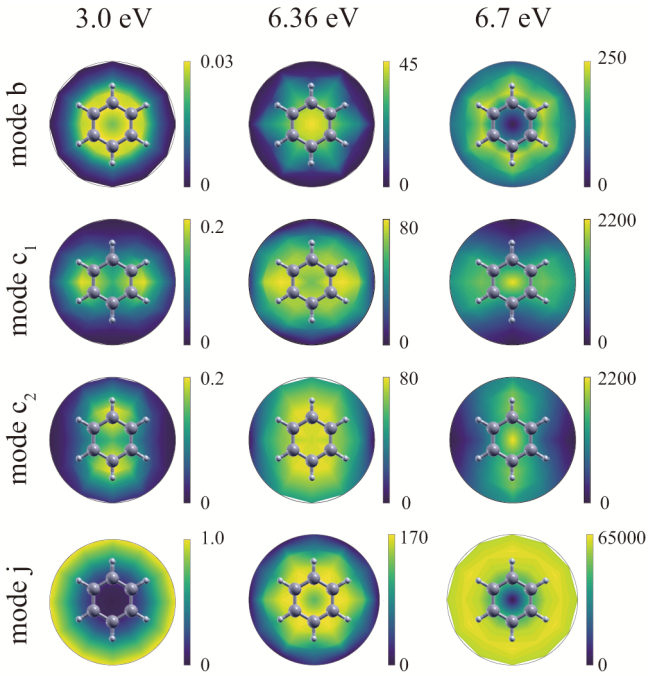

Figure 15: Off-resonance and on-resonance near-field Raman image mappings of modes $\boldsymbol{b}$, $\boldsymbol{c}_1$, $\boldsymbol{c}_2$, and $\boldsymbol{j}$

of benzene. The selection rule for off-resonance near-field Raman is well described in terms of the spatial structure of the near field and the molecular vibrations. The on-resonance Raman spectra are well analyzed by considering the transition dipole moments. For resonance near-field Raman, the $\pi - \pi^*$ transition of benzene at the equilibrium geometry is forbidden, but it is allowed at distorted structures due to vibronic couplings. Moving the tip position can lower the symmetry of the system, which changes the peak intensities as well as the contributing components. my method can treat the spatial structure of the near field explicitly, and provide an intuitive picture of the selection rule for near-field Raman spectroscopy.

Reference

[E1] K. Li et al., Nano Letters **17**, 3710 (2017).

[E2] E. Kazuma, J. Jung, H. Ueba, M. Trenary, and Y. Kim, Science **360**, 521 (2018).

[E3] B. Seemala et al., ACS Energy Letters **4**, 1803 (2019).

[E4] N. Tate and T. Yatsui, Scientific Reports **9**, 18383 (2019).

[E5] M. Osawa, K.-i. Ataka, K. Yoshii, and Y. Nishikawa, Applied Spectroscopy **47**, 1497 (1993).

[E6] P. L. Stiles, J. A. Dieringer, N. C. Shah, and R. P. Van Duyne, Annual Review of Analytical Chemistry **1**, 601 (2008).

[E7] T. Neuman, R. Esteban, D. Casanova, F. J. García-Vidal, and J. Aizpurua, Nano Letters **18**, 2358 (2018).

[E8] P. Verma, Chemical Reviews **117**, 6447 (2017).

[E9] B. Pettinger, P. Schambach, C. J. Villagómez, and N. Scott, Annual Review of Physical Chemistry **63**, 379 (2012).

[E10] F. Shao and R. Zenobi, Analytical and Bioanalytical Chemistry **411**, 37 (2019).

[E11] R. M. Stöckle, Y. D. Suh, V. Deckert, and R. Zenobi, Chemical Physics Letters **318**, 131 (2000).

[E12] M. S. Anderson, Applied Physics Letters **76**, 3130 (2000).

[E13] B. Pettinger, G. PICARDI, R. Schuster, and G. Ertl, Electrochemistry **68**, 942 (2000).

[E14] Z. Zhang, M. Sun, P. Ruan, H. Zheng, and H. Xu, Nanoscale **5**, 4151 (2013).

[E15] E. J. Ayars, H. D. Hallen, and C. L. Jahncke, Physical Review Letters **85**, 4180 (2000).

[E16] J. Steidtner and B. Pettinger, Physical Review Letters **100**, 236101 (2008).

[E17] C. Chen, N. Hayazawa, and S. Kawata, Nature Communications **5**, 3312 (2014).

[E18] R. Zhang et al., Nature **498**, 82 (2013).

[E19] J. Lee, K. T. Crampton, N. Tallarida, and V. A. Apkarian, Nature **568**, 78 (2019).

[E20] P. Liu, D. V. Chulhai, and L. Jensen, ACS Nano **11**, 5094 (2017).

[E21] X. Chen, P. Liu, Z. Hu, and L. Jensen, Nature Communications **10**, 2567 (2019).

[E22] S. Duan et al., Journal of the American Chemical Society **137**, 9515 (2015).

[E23] S. Duan, G. Tian, Z. Xie, and Y. Luo, The Journal of Chemical Physics **146**, 194106 (2017).

[E24] Z. Xie, S. Duan, G. Tian, C.-K. Wang, and Y. Luo, Nanoscale **10**, 11850 (2018).

[E25] S. Duan, Z. Xie, G. Tian, and Y. Luo, The Journal of Physical Chemistry Letters **11**, 407 (2020).

[E26] K. Fiederling et al., Nanoscale **12**, 6346 (2020).

[E27] J. Repp, G. Meyer, S. M. Stojković, A. Gourdon, and C. Joachim, Physical Review Letters **94**, 026803 (2005).

[E28] R. B. Jaculbia et al., Nature Nanotechnology **15**, 105 (2020).

[E29] T. Iwasa, M. Takenaka, and T. Taketsugu, The Journal of Chemical Physics **144**, 124116 (2016).

[E30] M. Takenaka, T. Taketsugu, and T. Iwasa, The Journal of Chemical Physics **152**, 164103 (2020).

[E31] T. Iwasa and K. Nobusada, Physical Review A **80**, 043409 (2009).

[E32] M. Thomas, F. Latorre, and P. Marquetand, The Journal of Chemical Physics **138**, 044101 (2013).

[E33] J. Mattiat and S. Luber, The Journal of Chemical Physics **149**, 174108 (2018).

[E34] L. Jensen, L. L. Zhao, J. Autschbach, and G. C. Schatz, The Journal of Chemical Physics **123**, 174110 (2005).

[E35] X. Andrade et al., Journal of Physics: Condensed Matter **24**, 233202 (2012).

[E36] K. Iida, M. Noda, K. Ishimura, and K. Nobusada, The Journal of Physical Chemistry A **118**, 11317 (2014).

[E37] E. B. Wilson, P. C. Cross, and J. C. Decius, *Molecular vibrations: the theory of infrared and Raman vibrational spectra*, Dover Publ., 1980.

[E38] A. D. Buckingham, Permanent and Induced Molecular Moments and Long-Range Intermolecular Forces, in *Advances in Chemical Physics*, edited by J. O. Hirschfelder, volume 12, pages 107–142, Wiley Online Library, 2007.

[E39] D. P. Craig and T. Thirunamachandran, Molecular Quantum Electrodynamics: An Introduction to Radiation-Molecule Interactions, 1998.

[E40] X. Andrade et al., Physical Chemistry Chemical Physics **17**, 31371 (2015).

[E41] J. P. Perdew, K. Burke, and M. Ernzerhof, Physical Review Letters **77**, 3865 (1996).

[E42] J. P. Perdew, K. Burke, and M. Ernzerhof, Physical Review Letters **78**, 1396 (1997).

[E43] D. R. Hamann, Physical Review B **88**, 085117 (2013).

[E44] K. Yabana and G. F. Bertsch, Physical Review B **54**, 4484 (1996).

[E45] R. Sinha-Roy, P. García-González, X. López Lozano, R. L. Whetten, and H.-C. Weissker, Journal of Chemical Theory and Computation **14**, 6417 (2018).

[E46] J. Jornet-Somoza and I. Lebedeva, Journal of Chemical Theory and Computation **15**, 3743 (2019).

[E47] L. Meng, Z. Yang, J. Chen, and M. Sun, Scientific Reports **5**, 9240 (2015).

[E48] R. Ahlrichs, M. Bär, M. Häser, H. Horn, and C. Kölmel, Chemical Physics Letters **162**, 165 (1989).

[E49] R. A. Kendall, T. H. Dunning, and R. J. Harrison, The Journal of Chemical Physics **96**, 6796 (1992).

[E50] Y. Li, J. Wan, and X. Xu, Journal of Computational Chemistry **28**, 1658 (2007).

[E51] J. Lorentzon, P.-e. Malmqvist, M. Flscher, and B. O. Roos, Theoretica Chimica Acta **91**, 91 (1995).

[E52] J. Neugebauer, M. Reiher, C. Kind, and B. A. Hess, Journal of Computational Chemistry **23**, 895 (2002).

[E53] D. Rappoport and F. Furche, The Journal of Chemical Physics **126**, 201104 (2007).

[E54] D. V. Chulhai and L. Jensen, The Journal of Physical Chemistry C **117**, 19622 (2013).

[E55] M. Takase et al., Nat. Photonics **7**, 550 (2013).

[E56] F. Santoro, C. Cappelli, and V. Barone, J. Chem. Theory Comput. **7**, 1824 (2011).

[E57] S. Duan, G. Tian, and Y. Luo, Journal of Chemical Theory and Computation **12**, 4986 (2016).

[E58] V. Mozhayskiy and A. Krylov, ezSpectrum, http://iopenshell.usc.edu/downloads.

[E59] D. A. Long, *The Raman effect: a unified treatment of the theory of Raman scattering by molecules*, John Wiley & Sons Ltd., Chichester, 2002.

[E60] Z. Xie, S. Duan, C.-K. Wang, and Y. Luo, The Journal of Physical Chemistry C **123**, 11081 (2019).

[E61] Y. Zhang et al., National Science Review **6**, 1169 (2019).

6 General conclusions

This thesis is devoted to elucidating the near-field effects on vibrational spectroscopy. With the development of the experimental equipment, there is a growing interest in the field of nano spectroscopy at the single molecular scale. My computational methods can evaluate the effect of the electric fields for high spatial resolution near-field vibrational spectroscopy well. By the combination of electromagnetic field calculation and electronic structure calculation, we can reach more realistic spectra and insight than conventional approaches.

In Chapter 3, I developed a computational method for near-field IR spectroscopy, which combines the first-principles quantum chemical calculation and the classical electromagnetic field calculation. The normal IR spectra, IRRAS, and SEIRAS of PNBA and MNBA are calculated by my method. For the modeling of electric fields around the metal nanoparticle, The electric field calculation proved that the near-field around the metal nano particle is almost uniform in molecular scale. The computational spectra supported the experimentally assumed selection rule.

In Chapter 4, to investigate the chemical effect of SERS, Raman spectra of 22BPY on the metal cluster is calculated. The DFT results show that 22BPY prefers co-planar adsorption on a (111) face with trans-conformation having close energy difference to cis-conformation. Binding to pure Au cluster is stronger than to pure Ag or Au–Ag alloy clusters, and adsorption onto the alloy surface can deform the surface. The computed Raman spectra are for pure Au, and Ag models match the experimental data well, indicating the need for dispersion interaction to reproduce strong Raman signal. This work provides insight into the 3D character of SERS on nano rough surfaces due to different binding energies and bond lengths of nanoalloys.

In Chapter 5, I developed a computational method for near-field Raman spectroscopy. The method can efficiently calculate on-/off-resonance Raman spectra. For demonstration, a model for the on-/off-resonance tip-enhanced Raman process in benzene was constructed. The obtained Raman spectra are well understood by considering both the

spatial structure of the near field and the molecular vibration in the off-resonance condition. For the on-resonance condition, the Raman spectra are governed by the transition dipole moment, in addition to the selection rule of off-resonance Raman. Interestingly, on-resonance Raman can be activated even when the near field forbids the transition at equilibrium geometry due to vibronic couplings originating from structural distortions. In addition, the vibrational mode dependency of Raman 2D mapping is clearly observed, and excitation-wavelength dependency is also observed.

In this thesis, I clarified the selection rules for near-field IR and Raman derived from the spatial structure of the near field by taking typical experiments as examples. The computational methods developed in this thesis is good in that they can be in general use, and the computational cost of multipolar Hamiltonian is marginal. In the method developed in the thesis, we ignored backward effects, in which an excited molecule affects the near-field. Ideally, molecule and near-field source should be treated self-consistently. Also ignored in the current formulation is the magnetic interactions as these effects are very weak in the present studies. In the future, these issues should be addressed.

Acknowledgement

All the studies in this thesis were carried out under Professor Tetsuya Taketsugu, Department of Chemistry, Faculty of Science, Hokkaido University. I would like to express my sincere appreciation to Professor Taketsugu for suggestive advices, discussions, and generous help.

I would like to represent my sincere gratitude to my supervisor, Assistant professor Takeshi Iwasa, for all his help and support during six years throughout the course of this work.

I would like to express my sincere thanks to Associate Professor Masato Kobayashi, Associate Professor Ryo Wakeshima, Specially Appointed Associate Professor Andrey Lyalin, Specially Appointed Assistant Professor Kenichiro Saita, Specially Appointed Assistant Professor Yuriko Ono, Dr. Takao Tsuneda, and Dr. Tomoko Akama for practical advice and fruitful discussion in our weekly seminars.

I would like to thank all of the present and former members of our group for providing a pleasant working atmosphere.

I wish to thank Professor Kei Murakoshi, Professor Satoshi Maeda, and Associate professor Shin-ichiro Sato for serving my dissertation committee sincerely.

I wish to express my appreciation to Dr. Masatoshi Osawa for fruitful discussions about the contents in Chapter 3. I also would like to show my appreciation to Mr. Yoshikazu Hashimoto, Dr. Gediminas Seniutinas, Dr. Armand Balčytis, Professor Saulius Juodkazis, and Associate Professor Yoshiaki Nishijima for the electromagnetic field calculation part and the experimental part of the collaborative research in Chapter 4. I express deep gratitude to Dr. Yousoo Kim, Dr. Hiroshi Imada, and Dr. Rafael Jaculbia, as well as to Drs. Norihiko Hayazawa, Emiko Kazuma, Kuniyuki Miwa, and Bo Yang for the collaborative research related to Chapter 5.

I thank the financial support by “the Research fellowship for young scientists by the Institute for Quantum Chemical Exploration (IQCE)”.

Finally, I would like to thank my family for their encouragement and understanding.